

Laboratory landquakes: Insights from experiments into the high-frequency seismic signal generated by geophysical granular flows

Matthew Iain Arran^{1,2}, Anne Mangeney^{1,2}, Julien de Rosny^{3,4}, Maxime Farin^{4,5}, Renaud Toussaint^{6,7}, and Olivier Roche^{8,9}

¹Institut de Physique du Globe de Paris

²Université de Paris, Institut de physique du globe de Paris, CNRS, F-75005 Paris, France

³Laboratoire Ondes et Acoustique

⁴Laboratoire Ondes et Acoustique, Institut Langevin, ESPCI Paris, PSL University, CNRS, 75005 Paris, France

⁵Institut Langevin

⁶Institut de Physique du Globe de Strasbourg

⁷Université de Strasbourg, CNRS, Institut Terre et Environnement de Strasbourg, UMR 7063, F-67084 Strasbourg, France

⁸Laboratoire Magmas et Volcans (Université Clermont Auvergne-CNRS-IRD)

⁹Université Clermont Auvergne, CNRS, IRD, OPGC, Laboratoire Magmas et Volcans, F-63000 Clermont-Ferrand, France

November 30, 2022

Abstract

Geophysical granular flows exert basal forces that generate seismic signals, which can be used to better monitor and model these severe natural hazards. A number of empirical relations and existing models link these signals' high-frequency components to a variety of flow properties, many of which are inaccessible by other analyses. However, the range of validity of the empirical relations remains unclear and the models lack validation, owing to the difficulty of adequately controlling and instrumenting field-scale flows. Here, we present laboratory experiments investigating the normal forces exerted on a basal plate by dense and partially dense flows of spherical glass particles. We measured the power spectra of these forces and inferred predictions for these power spectra from the models for debris flows' seismic signals proposed by Kean et al. (2015), Lai et al. (2018), and Farin, Tsai, et al. (2019), using Hertz theory to extend Farin, Tsai, et al. (2019)'s models to higher frequencies. Comparison of our observations to these predictions, and to predictions derived from Bachelet (2018) and Bachelet et al. (2021)'s model for granular flows' seismic signals, shows those of Farin, Tsai, et al. (2019)'s 'thin-flow' model to be the most accurate, so we examine explanations for this accuracy and discuss its implications for geophysical flows' seismic signals. We also consider the normalisation, by the mean force exerted by each flow, of the force's mean squared fluctuations, showing that this ratio varies by four orders of magnitude over our experiments, but is determined by the bulk inertial number of the flow.

Laboratory landquakes: Insights from experiments into the high-frequency seismic signal generated by geophysical granular flows

M. I. Arran¹, A. Mangeney¹, J. De Rosny², M. Farin², R. Toussaint^{3,4}, O. Roche⁵

¹Université de Paris, Institut de physique du globe de Paris, CNRS, F-75005 Paris, France

²Institut Langevin, ESPCI Paris, PSL University, CNRS, 75005 Paris, France

³Université de Strasbourg, CNRS, Institut Terre et Environnement de Strasbourg, UMR 7063, F-67084 Strasbourg, France

⁴SFF PoreLab, The Njord Centre, Department of Physics, University of Oslo, Oslo, Norway

⁵Université Clermont Auvergne, CNRS, IRD, OPGC, Laboratoire Magmas et Volcans, F-63000 Clermont-Ferrand, France.

Key Points:

- We conducted novel laboratory experiments to test five existing models for the high-frequency seismic signals generated by granular flows
- The ‘thin-flow’ model of Farin, Tsai, et al. (2019) was the most accurate and makes predictions consistent with empirical observations
- The ratio between the mean and fluctuating forces exerted by a granular flow varies greatly, determined by an inertial number of the flow

Corresponding author: Matthew Arran, arran@ipgp.fr

Abstract

Geophysical granular flows exert basal forces that generate seismic signals, which can be used to better monitor and model these severe natural hazards. A number of empirical relations and existing models link these signals' high-frequency components to a variety of flow properties, many of which are inaccessible by other analyses. However, the range of validity of the empirical relations remains unclear and the models lack validation, owing to the difficulty of adequately controlling and instrumenting field-scale flows. Here, we present laboratory experiments investigating the normal forces exerted on a basal plate by dense and partially dense flows of spherical glass particles. We measured the power spectra of these forces and inferred predictions for these power spectra from the models for debris flows' seismic signals proposed by Kean et al. (2015), Lai et al. (2018), and Farin, Tsai, et al. (2019), using Hertz theory to extend Farin, Tsai, et al. (2019)'s models to higher frequencies. Comparison of our observations to these predictions, and to predictions derived from Bachelet (2018) and Bachelet et al. (2021)'s model for granular flows' seismic signals, shows those of Farin, Tsai, et al. (2019)'s 'thin-flow' model to be the most accurate, so we examine explanations for this accuracy and discuss its implications for geophysical flows' seismic signals. We also consider the normalisation, by the mean force exerted by each flow, of the force's mean squared fluctuations, showing that this ratio varies by four orders of magnitude over our experiments, but is determined by the bulk inertial number of the flow.

Plain Language Summary

Landslides, like earthquakes, generate seismic signals: vibrations of the earth that can be detected a long way away. Analysis of the most rapid vibrations could provide information about how large a landslide is or how damaging it will be, helping emergency services respond. But full-size landslides are complex and difficult to study, so the generation of these vibrations is not yet sufficiently well understood for this information to be reliable. Therefore, in the place of full-size landslides, we studied simplified, small-scale versions in the laboratory, testing previous authors' predictions for the seismic signals they generate. We find that one set of predictions was particularly accurate and show that the corresponding predictions for full-size landslides are consistent with previous observations. This implies that a landslide's seismic signal can be used to calculate its size, its speed, and the typical size of particles within it.

1 Introduction

1.1 Background

Landslides and other geophysical granular flows are a major natural hazard, causing on average 4,000 deaths worldwide each year from 2004 to 2016 (Froude & Petley, 2018) and an estimated billions of dollars of annual damage in the United States alone (Fleming et al., 1980; National Research Council, 1985; Schuster & Fleming, 1986). Few areas have an early warning system in place (Guzzetti et al., 2020) and a damaging event's magnitude and effects may remain unknown for hours or days after it happens (Hervás, 2003; Scholl et al., 2017), hindering the response of emergency services. Modelling is currently unable to remedy these knowledge gaps or to accurately identify the hazardous areas that should be avoided, with poorly constrained parameters, such as a flow's basal friction coefficient, being important in determining a landslide's runout (van Asch et al., 2007; Lucas et al., 2014; Delannay et al., 2017; Cuomo, 2020).

Better monitoring of landslide-prone areas and better modelling of flows' evolution are therefore key to the reduction of landslide hazard, and the use of seismic signals is a promising tool towards these aims. Geophysical flows exert forces on the

ground over which they travel, resulting in the outwards-propagating seismic waves that Kanamori and Given (1982) first described in detail, for a rock avalanche at Mount St. Helens. These seismic waves, which we refer to as ‘landquakes’, can be detected by a local or regional seismic network, permitting continuous monitoring of a wide area. This monitoring suggests the possibility of early warning systems, analogous to those in use and development for earthquakes (e.g. Given et al., 2018). Furthermore, landquakes encode information about a landslide’s magnitude and evolution over time, and so these seismic signals can be analysed to assess damage, to constrain model parameters, and to compare different models.

However, the low-frequency components of landquakes studied by Kanamori and Given (1982) can typically only be detected for large landslides ($> 10^7 \text{ m}^3$ according to Allstadt et al. (2018)) and are predominantly generated by the accelerations of a landslide’s centre of mass (Kawakatsu, 1989; Dahlen, 1993; Fukao, 1995). Therefore, even when detected, they cannot provide information on many properties relevant to landslide modelling and harm assessment, such as the size of individual particles within the flow or the vertical profiles of flow properties.

To extract more information and infer these properties, previous authors suggest using the high-frequency component of landquakes, generated by the rapidly fluctuating forces exerted by the flow and associated with the accelerations of individual particles within it. The spectrogram of this high-frequency component and its envelope have distinctive shapes (Suriñach et al., 2005) which can be used to detect landslides (e.g. Hibert et al., 2014; Dammeier et al., 2016; Fuchs et al., 2018; Lee et al., 2019). Furthermore, the properties of this envelope can be related to those of the landslide: the envelope’s duration to the landslide’s duration and hence its loss of potential energy (Deparis et al., 2008; Hibert et al., 2011; Levy et al., 2015); the envelope’s amplitude to the seismic energy emitted by the landslide and hence its volume (Norris, 1994; Hibert et al., 2011; Levy et al., 2015), its work rate against friction (Schneider et al., 2010; Levy et al., 2015), and its momentum (Hibert et al., 2015, 2017); and envelope scale and shape parameters to the landslide’s geometry via multilinear regression (Dammeier et al., 2011). Some of these relations have been replicated in laboratory experiments on dry granular flows: Farin et al. (2018) links seismic envelopes’ duration to potential energy loss and envelopes’ shape to flows’ varying vertical and horizontal momenta, for collapses of granular columns on angled planes, while Farin, Mangeney, et al. (2019) proposes an expression for a collapse’s net seismic energy emission, in terms of the column’s mass, aspect ratio, particle diameter, and maximum centre of mass velocity.

Other laboratory experiments have investigated the dynamics by which granular flows generate high-frequency signals, in geometries including discharging silos (Gardel et al., 2009), rotating drums (Hsu et al., 2014), and rotary shear cells (Taylor & Brodsky, 2017). Gardel et al. (2009), calculating the power spectra of the forces that flows exert on their boundaries, shows the amplitude of high-frequency force fluctuations to increase with increasing flow rate. Hsu et al. (2014), meanwhile, shows the typical magnitude of such fluctuations to increase with increases in flow rate and grain size, with the mean force exerted over macroscopic flow timescales, and with the shear-determined ‘inertial stress’ σ_i , as approximately $\sigma_i^{0.5}$ for flows of water-saturated gravel. This is broadly consistent with Taylor and Brodsky (2017)’s observation that, under constant mean pressure, granular flows’ force fluctuations induced boundary vibrations with squared amplitude proportional to $d^3 I$, for grain diameter d and estimate I of the ‘inertial number’: a local, non-dimensional shear rate, with its square equal to the ratio between the inertial stress and the mean stress, that previous authors suggest will uniquely determine all other local, non-dimensional flow parameters (GDR MiDi, 2004; da Cruz et al., 2005; Jop et al., 2006).

However, there are discrepancies between the relations suggested by different authors, including the difference between a landslide’s momentum and its work against friction, and different exponents in power laws for force fluctuations’ amplitude as a function of I . Furthermore, the relations are empirical, so both their precision and their range of validity are unclear. Allstadt et al. (2020)’s large-scale experiments, for example, identify no simple relations between the properties of debris flows and of the fluctuating forces they exert, despite excellent instrumentation. To reliably link landslides’ properties to those of the high-frequency seismic signals they generate, a mechanistic model for landquake generation is required.

1.2 Existing Models

Models of the high-frequency component of landquakes rely on the same framework: consideration of the total seismic signal as a sum of the uncorrelated signals generated by individual, random particle impacts, with i) the properties of the impacts determined by some mean properties of the particulate flow and ii) a specified Green’s function mapping the force of an individual impact to the seismic signal observed at a remote station. This stochastic impact framework arises from Tsai et al. (2012)’s model of seismic noise generation from riverine sediment transport, and Gimbert et al. (2019) validates it in that context using flume experiments. We discuss its validity for landquakes in S2, showing that it will be applicable to any extensive flows of stiff particles for which energetic impacts are more significant than other high-frequency sources, for signal periods smaller than the timescales over which the bulk flow varies. Examples may include avalanches, the coarse-grained fronts of debris flows, and rockfalls involving multiple blocks.

Assuming the framework’s validity, prediction of a flow volume V ’s high-frequency landquake signal requires consideration of the locations $\mathbf{x} \in V$ of signal generation, and the specification of just three things at each location: 1) the number $n_I(\mathbf{x})$ of impacts per unit volume and time; 2) the force $\mathbf{F}_I(\mathbf{x}, t)$ applied by a single, typical impact over its duration; and 3) the Green’s function $\mathbf{G}(t, \mathbf{r}; \mathbf{x})$ for each single-component velocity response $v_{\mathbf{r}}(t)$ to that force of the seismic station detecting the signal, located at \mathbf{r} . Writing $\tilde{\cdot}$ for Fourier transforms over time Δt , the landquake signal will then have power spectral density

$$P_{v_{\mathbf{r}}}(f) = |\tilde{v}_{\mathbf{r}}(f)|^2 / \Delta t = \int_V n_I(\mathbf{x}) |\tilde{\mathbf{F}}_I(\mathbf{x}, f) \cdot \tilde{\mathbf{G}}(f, \mathbf{r}; \mathbf{x})|^2 d^3\mathbf{x}. \quad (1)$$

1.2.1 Direct Use of Tsai et al. (2012)

Kean et al. (2015), Lai et al. (2018), and Farin, Tsai, et al. (2019) consider only impacts at the base of a flow to be significant in signal generation, and assume 1) that the rate of impacts is determined by the advection of particles, with the mean flow, into basal irregularities of the same scale; 2) that the force a particle exerts varies over timescales much shorter than the range of periods to which the seismic station is sensitive; and 3) that the relevant Green’s function is that for Rayleigh-wave propagation to the far field. Under these assumptions, if a representative impacting particle has diameter d and downslope speed u , it will have collision rate u/d , so that a bedrock-contacting flow area A in which impacting particles have a volume fraction ϕ will have an approximate integrated collision rate $\int_V n_I d\mathbf{x} = \phi Au/d^3$. For all signal periods of interest, the typical force applied by an impact will be approximable as a Dirac delta function in time and hence constant in the frequency domain, equal to the impulse transferred, so that $\tilde{\mathbf{F}}_I(f) = \Delta p \mathbf{e}_I$ for a representative impulse magnitude Δp and unit vector \mathbf{e}_I . Meanwhile, the relevant frequency-space Green’s function for a station at radius r will have magnitude $|\mathbf{e}_I \cdot \tilde{\mathbf{G}}| = R(f)e^{-\alpha(f)r}/\sqrt{r}$, for functions R and α related to Rayleigh-wave propagation and inelastic attenuation, respectively

(Lamb, 1904). Consequently, the signal’s power spectral density will be

$$P_{v_r}(f) = \frac{\phi A u \Delta p^2}{d^3 r} R(f)^2 e^{-2\alpha(f)r}. \quad (2)$$

Material above the flow’s base is supposed to affect the signal only via its influence on u and Δp .

Kean et al. (2015) suggests that u scales with the measured surface velocity and Δp with the mean stress exerted by the flow, equal to the base-normal component of the flow’s local weight per unit area. The authors use an empirical, piecewise-continuous function α , and avoid consideration of scaling constants, ϕ , R and d by examining only the ratio of $P_{v_r}(f)$ to that measured during a reference debris flow in the same channel, for which such parameters are assumed to be the same. The paper uses this model to estimate the depths of static sediment ‘shielding’ the channel centre from impacts, and these estimates correctly remain positive, but the paper performs no further evaluation of the model.

Lai et al. (2018) suggests that large, flow-depth-spanning particles dominate the signal, so that d should be the 94th percentile of the particle diameter distribution and u should be the depth-averaged downslope velocity \bar{u} of the flow. The authors implicitly take $\phi = 1$ and further assume that impacts transfer an impulse equal to that for elastic rebounds of individual near-spherical particles at vertical velocity \bar{u} , such that $\Delta p = \pi \rho d^3 \bar{u} / 3$ for particle material density ρ . Equations for $R(f)$ and $\alpha(f)$ are taken from Tsai et al. (2012), Tsai and Atiganyanun (2014), and Gimbert and Tsai (2015), and then applied to a Californian debris flow, to invert the peak frequency of $P_{v_r}(f)$ for r . However, this inversion relies on the model for signal generation only via the assumption that $|\tilde{\mathbf{F}}_I(f)|$ is independent of f in the frequency range of interest, so this assumption is the only part of the model that the paper tests. Values for A , u , and d were inferred but not measured.

Farin, Tsai, et al. (2019) generalises the model of Lai et al. (2018) to different flow regions and regimes and to a continuous particle size distribution. The authors calculate that the impacts of particles falling from the flow front or saltating ahead of it are less significant for signal generation than those in the flow’s dense snout and body. In these two regions, for ‘thin’ flows of depth h comparable to the largest particle diameters, the paper suggests that the Lai et al. (2018) model will hold, with slight modifications: ϕ is explicitly stated; there are extra terms in the equation for Δp to account for inelasticity and variation in the angle and velocity of impacts; R is adjusted to account for non-vertical \mathbf{e}_I ; and d is represented by its appropriately weighted average over the distribution of particle diameters, which is suggested to be approximately equal to the 73rd percentile of that distribution. However, for ‘thick’ flows, where h is much larger than the particles’ diameters, the paper suggests that, in addition to the above slight modifications, the relevant advection and impact velocity is that of base-adjacent particles. Assuming no basal slip, in the sense that velocities tend to zero towards the flow’s base, u is then proportional to $\bar{u}d/h$ and the representative value of d is equal to the 86th percentile of the particle diameter distribution. The authors tested neither of the ‘thin-flow’ and ‘thick-flow’ models.

1.2.2 Model of Bachelet et al.

In contrast to the above papers, Bachelet (2018) and Bachelet et al. (2021) consider impacts between different layers of particles, throughout the depth of the flow, and suppose 1) that the local impact rate is the rate at which adjacent layers shear over each other; 2) that the force throughout an impact is described by Hertz theory with typical impact velocity equal to the standard deviation in particle velocity

within each layer; and 3) that the Green’s function includes exponential attenuation of the force with the impact’s distance from the flow’s base.

The use of Hertz theory to describe the contact force between impacting particles, detailed in S3, predicts the duration of impacts and so a frequency scale for the spectral density of the forces they exert (Hertz, 1881). For a collision at relative normal velocity u_n between two spherical particles of diameter d , consisting of material with density ρ , Young’s modulus E , and Poisson’s ratio ν , Hertz theory predicts a timescale for the impact

$$\tau = \left[\frac{\pi^2 \rho^2 (1 - \nu^2)^2}{4E^2 u_n} \right]^{1/5} d. \quad (3)$$

With this τ , the spectral density of the normal force between the particles is

$$|\tilde{F}_I(f)|^2 = \left(\frac{\pi \rho d^3 u_n}{3} \right)^2 \zeta(\tau f) \quad (4)$$

for a non-dimensional function $\zeta(\tau f)$, plotted in Figure S1b, which is approximately equal to 1 for $\tau f \ll 1$, monotonically decreases to $\zeta(\tau f_c) = 0.5$ for non-dimensional corner frequency $\tau f_c \approx 0.208$, and is much less than 1 for $\tau f > 1$. Impacts at higher velocities u_n apply forces with higher spectral density, over a wider frequency range.

This spectral density doesn’t appear explicitly in Bachelet (2018) or Bachelet et al. (2021), which instead use the integral of ζ over all f to consider the total seismic power generated by a flow. However, we can follow the authors’ reasoning to derive from equation (4) a prediction for the spectral density of a flow’s high-frequency landquake signal, in the form of equation (1). First, separating a flow with representative particle size d and particle volume fraction ϕ into layers, and writing z_j for the vertical position of each layer and u_j for the mean horizontal velocity within it, the authors suggest that the rate of impacts is

$$n_I(\mathbf{x}) = \frac{4\phi}{\pi d^3} \sum_j (u_j - u_{j-1}) \delta(z - z_j) \quad (5)$$

for Dirac delta function δ . Then, writing T_j for the granular temperature in the j th layer, equal to the variance of individual particles’ velocities, the authors take the spectral density of the force applied by a typical impact to be given by equation (4) with impact velocity $u_n = \sqrt{T_j}$. Finally, the magnitude of the frequency-space Green’s function for an impact at height z is taken to be $e^{-\gamma z/2} |\tilde{G}_b|$, where γ is an attenuation constant and $|\tilde{G}_b|$, describing a measurement station’s velocity response to vertical basal forces, is constant due to the assumption of an incoherent, diffuse seismic field with constant attenuation. Therefore, a flow of area A will generate a landquake signal with power spectral density

$$P_{v_r}(f) = \frac{4\phi A}{\pi d^3} |\tilde{G}_b|^2 \sum_j (u_j - u_{j-1}) \Delta p_j^2 \zeta(\tau_j f) e^{-\gamma z_j} \quad (6)$$

for

$$\Delta p_j = \frac{\pi \rho d^3 \sqrt{T_j}}{3}, \quad \tau_j = \left[\frac{\pi^2 \rho^2 (1 - \nu^2)^2}{4E^2 \sqrt{T_j}} \right]^{1/5} d. \quad (7)$$

The experiments described by both Bachelet (2018) and Bachelet et al. (2021) show this model to be consistent with measurements of the seismic signals generated by approximately steady and uniform laboratory-scale granular flows, but the results are not conclusive. Releasing flows of $d = 2$ mm-diameter glass beads in a channel inclined at angles between 16.5° and 18.1° , accelerometers were used to estimate the total seismic power imparted to an isolated plate by overlying flows of depths between

15d and 20d, and this power was compared to the prediction of equation (6), with flow parameters estimated using high-speed photography through the channel's transparent sidewalls. The agreement is reasonable, but is highly dependent on the fitted parameter γ , and so the number of estimates, and their range of variation, are too small for conclusions to be definitive. The use of Hertz theory permits predictions for the frequency-dependence of the power spectral density, but no such predictions are compared with experimental results. Further tests are therefore required.

1.3 Aim of Our Work

Given their insufficient validation to date, our work aims to test the above models of high-frequency landquake signal generation. Because we are concerned with the generation of the signal, rather than its propagation, we consider models' predictions for the power spectral density P_F of the total base-normal force exerted by the flow, which may be obtained by removing the Green's function in equation (1), so by dividing equation (2) by $R^2 e^{-2\alpha r}/r$ and equation (6) by $|\tilde{G}_b|^2$. P_F will be proportional to the spectral density of the signal at a receiver, with its appropriately weighted integral proportional to the seismic power transmitted by the flow, but P_F , unlike these measurements, is independent of the response of the base on which the flow propagates.

However, it is difficult to use field-scale granular flows to test the models' predictions for P_F . Natural geophysical flows often occur in remote locations, infrequently and unpredictably, and so the sites of most flows are not instrumented for any measurements of flow parameters. Where sites are instrumented, the destructiveness of geophysical flows restricts which parameters can be measured, excluding most used by the above models. Furthermore, geophysical flows are typically extremely unsteady and heterogeneous, so that any given landquake signal may be produced by a flow region with parameters very different from those that have been measured. Finally, the inference from a landquake signal of the forces that generated it requires inversion of the Green's function, which is typically poorly constrained at the high frequencies of interest, and to which the inversion is typically very sensitive at precisely these high frequencies.

We therefore conducted laboratory experiments to link the properties of a granular flow to the seismic signal it generates. In the laboratory, flows can be fully controlled and instrumented, allowing a wide range of parameter values to be explored and measured. Apparatus can be designed to produce steady, fully developed, homogeneous flows, and the Green's function can be well constrained over a large frequency range by calibration. Since the models entirely neglect geophysical flows' fluid phases and consider normal impulses transferred between similarly sized particles, they can be tested with the dry flows of monodisperse, spherical grains that best satisfy their assumptions. Having established the relevant physics for simple flows, the applicability of results to more complex, geophysical flows can be discussed.

We describe our laboratory experiments in section 2.1, our analysis of experimental data in section 2.2, and our calculation of existing models' predictions for flows' force signals P_F in section 2.3. Section 3.1 describes how each flow's signal evolves with the flow, over the course of an experiment, while section 3.2 describes the properties of P_F and section 3.3 compares those properties to the models' predictions. We discuss the implications of this comparison for our flows' velocity profiles in section 4.1, and the relation between non-dimensional shear and non-dimensionalised force fluctuations in section 4.2, while section 4.3 discusses the application of our results to geophysical flows, including the effects of different Green's functions, particle size and polydispersity, and flow evolution. Section 5 concludes by summarising our results.

2 Methods

2.1 Experimental Apparatus

As the simplest possible analogue of a geophysical granular flow, we studied the flow of spherical glass beads, $d = 2$ mm in diameter, in an inclined channel 2.5 m long and $W = 0.2$ m wide, shown in Figure 1. The beads were 1.7–2.1 mm Type S glass beads produced by Sigmund Lindner GmbH and provided by MINERALEX, with material density $\rho = 2500 \text{ kg m}^{-3}$ and Young’s modulus $E = 63 \text{ GPa}$ (Sigmund Lindner, 2018). In each experiment, 40 kg of beads were initially stored in a plastic reservoir of volume 0.08 m^3 , from which they flowed out via a rectangular opening of width 0.18 m and adjustable height h_g , controlled to within 0.06 mm by a plastic gate which was fixed in place during each experiment. A separate plastic release gate blocked this opening before each experiment and was manually lifted to start outflow. On leaving the reservoir, beads entered the separately supported channel, which had an aluminium base; transparent, 0.1 m-high acrylic walls; and an incline $\tan \theta$, which could be adjusted by changing the heights of the braces attaching the channel to its supports. The channel’s base was roughened with the same type of glass beads as constituted the flow, fixed in place with extra-strong double-sided carpet tape, with an irregular, dense pattern achieved by random pouring.

The flow of beads down the channel adapted to these conditions over a distance of 1.92 m, before reaching a rectangular, instrumented steel plate set into a corresponding hole in the centre of the channel’s base. The plate was $X = 0.18$ m long, $Y = 0.1$ m wide, and $H = 2$ mm thick, with its surface flush with that of the aluminium base to within 0.02 mm and separated from it by an isolation gap of 0.04 ± 0.01 mm, achieved by using strips of plastic film as spacers during emplacement. The plate was supported by a force sensor and a support piece, with the three separated by washers and held together by a prestressing screw, the head of which was glued into a 0.5 mm-deep recess in the centre of the plate’s underside. The support piece, in turn, was attached to the channel’s substructure using phenyl salicylate (salol), which was added to the join when molten and solidified to form a stiff connection, but could be melted with a heat gun for removal of the plate or adjustment of its position. Before the plate’s emplacement, we used the same salol to roughen its surface with glass beads: heating the plate, we added salol to form a thin, liquid layer, and we poured beads on top to form an irregular, dense pattern, before the salol solidified and fixed them in place.

After the plate, the flow of beads continued for 0.4 m, before flowing out of the channel and into a plastic outflow tray. Plastic sheeting extended the tray’s walls, to prevent energetic particles from escaping.

Four sets of devices took measurements of the flow: a mass balance beneath the outflow tray; the force sensor supporting the instrumented plate; four accelerometers attached to the plate’s underside; and a high-speed camera directed through the channel’s wall. The mass balance was a Dymo S50 digital shipping scale, which measured in each experiment the cumulative mass that had passed through the channel. The force sensor was a Kistler 9027C three-component force sensor and was connected to a Kistler 5073 charge amplifier, measuring the normal, downslope, and cross-slope forces exerted by the flow on the plate. The accelerometers were Brüel and Kjær type 8309 accelerometers, attached with salol to randomly selected positions on the plate’s underside and connected to a Brüel and Kjær Nexus 2692-A-OS4 conditioning amplifier, to measure the normal vibrations of the plate and hence the seismic energy imparted to it by the flow. Settings of the force sensor and accelerometer amplifiers are described in S4. The camera was an Optronis CR600x2, with a Sigma 17–50 mm F2.8 EX DC lense, and was level with and focussed on the inside of the channel sidewall, directly cross-slope from the instrumented plate’s centre. The camera’s inclination was the same as the channel’s and its field of view was 640×256 pixels, corresponding

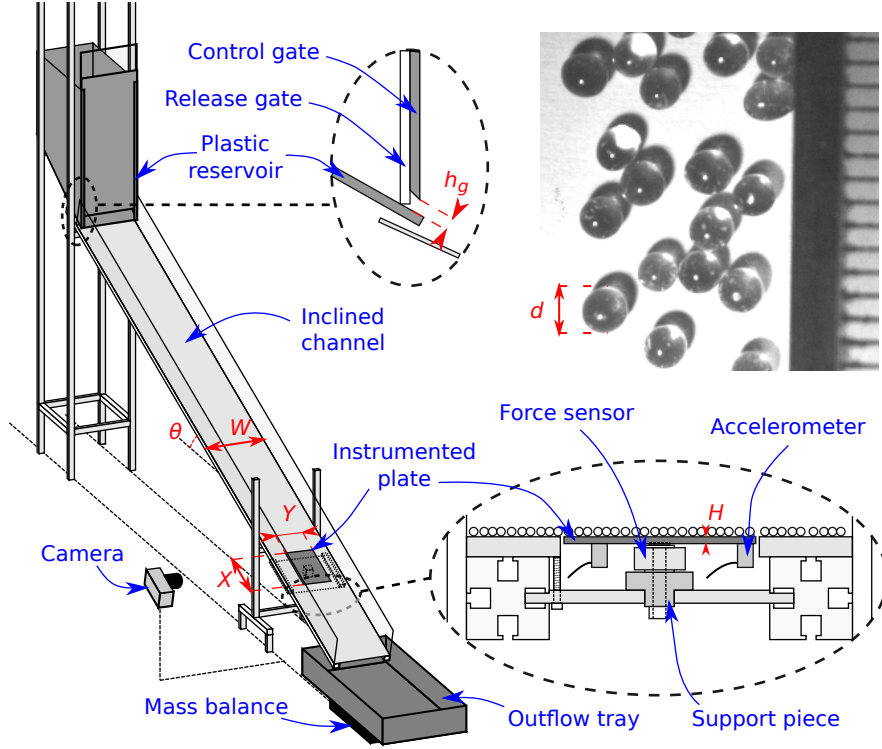


Figure 1. *Schematic of experimental apparatus.* Experiments are conducted in the channel represented, to scale, at left, with components of the apparatus labelled in blue and relevant dimensions in red. Expansions at top-centre and bottom-right represent, in cutaway views and not to scale, details of the reservoir and the instrumented plate, respectively. The glass beads used in experiments are shown at top-right, with a mm-unit scale.

to a region 8 cm long and 3.2 cm high. The sidewall was lit using a Photonlines H5 LED light, via a white sheet of paper which acted as a reflective diffuser, and we used an exposure of 250 μ s and a frame rate of 2000 s^{-1} .

To control the measurement devices, we used an Arduino Uno R3 microcontroller board, and we recorded measurements using a Pico Technology Picoscope 4824 oscilloscope connected to a Lenovo E530 laptop. Measurements from the mass balance, force sensor, and accelerometers were recorded from the time $t = 0$ at which the reservoir's release gate was lifted until the outflow stopped at $t = t_e$, while the camera recorded footage over a duration Δt_c between 2 s and 10 s, after a delay time t_d in which the flow developed into a steady state. Details are in S5.

We conducted experiments with six different channel inclinations between 22.8° and 27.5° ($\tan \theta = 0.42, 0.44, 0.46, 0.48, 0.50$ and 0.52), with this order randomised to negate the effect of any systematic variation in atmospheric conditions or measurement sensitivity. For each inclination, we conducted three repeats with the reservoir control gate at each of four different heights ($h_g = 5$ mm, 10 mm, 20 mm and 40 mm), with the order of gate heights again selected at random.

At channel inclines equal to and greater than $\tan \theta = 0.46$ ($\theta = 24.7^\circ$), there was a gate height below which flows were in the gaseous regime of e.g. Börzsönyi and Ecke (2006) and Taberlet et al. (2007), with all glass beads in saltation and accelerating downslope. We recorded no measurements of such flows, which were energetic and far

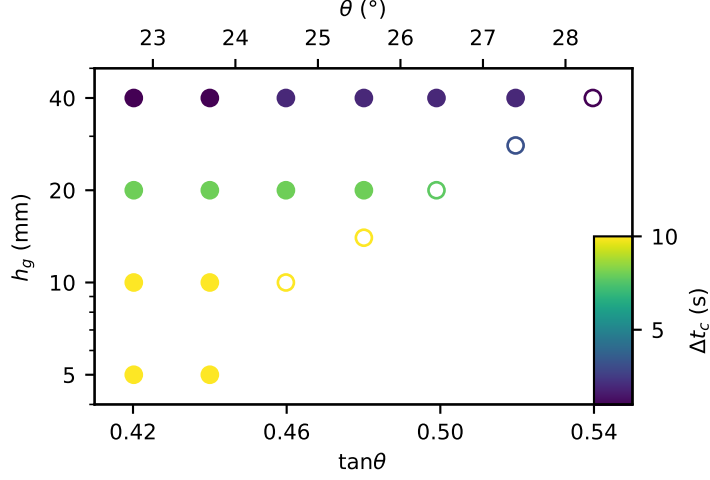


Figure 2. Channel inclines $\tan \theta$ and release gate heights h_g used in experiments. \circ indicates an experiment for which the flow was in the transitional regime, while colours indicate the duration of time Δt_c recorded by the camera.

from stationary, with a large number of beads escaping across the channel’s sidewalls and with the camera’s images unusable for reliable measurements. At each such incline, we instead recorded measurements at all gate heights resulting in dense flows and at one gate height resulting in a ‘transitional-regime’ flow, with a dense basal flow below a saltating layer. These gate heights are plotted in Figure 2, within the full parameter space investigated.

2.2 Data Analysis

For each experiment within the parameter space, we analysed the experimental data to calculate dynamic, seismic, and kinematic properties of the flow: the mass of particles that lay over the instrumented plate and the effective friction coefficient between the two; the mass flux of particles through the channel and their average velocity; the power spectrum of the normal force exerted on the plate by the flow; and the vertical profiles of particle volume fraction, velocity, and granular temperature at a channel wall. We recall that W denotes the channel’s width and θ its angle of inclination; that X , Y , and H denote the length, width, and thickness of the plate; and that t_d and Δt_c denote the delay before and the duration of the high-speed camera’s recording, respectively. These and all other variables are listed in S1 and all code used to perform these analyses is available at Arran et al. (2021).

To infer the mass overlying the plate and its effective friction coefficient with the flow, we used the data from the force sensor. Averaging over successive 0.5 ms intervals, the net downslope force $F_x(t)$ and plate-normal, downwards force $F_z(t)$ applied to the plate by the flow were calculated from the voltage output of the force sensor’s charge amplifier, as described in S6. Then, assuming no net plate-normal acceleration of the flow overlying the plate, over the period of steady flow recorded by the camera, we calculated the average mass per unit area overlying the plate as

$$\sigma = \frac{\langle F_z \rangle_{\Delta t_c}}{XYg \cos \theta}, \quad (8)$$

where $\langle \cdot \rangle_{\Delta t_c}$ represents the arithmetic mean over $t_d < t < t_d + \Delta t_c$ and g represents gravitational acceleration. Similarly, we followed Hungr and Morgenstern (1984) and

Roche et al. (2021) in calculating the effective friction coefficient as

$$\mu = \frac{\langle F_x \rangle_{\Delta t_c}}{\langle F_z \rangle_{\Delta t_c}}, \quad (9)$$

with this calculation validated in S6, section S6.3.

To calculate the mass flux through the channel, we examined the data recorded by the mass balance. Having the cumulative mass $M(t)$ that had flowed through the channel after time t , we calculated the average flux per unit channel width, over the period of steady flow recorded by the camera, as

$$q = \frac{M(t_d + \Delta t_c) - M(t_d)}{\Delta t_c W}. \quad (10)$$

Assuming this average mass flux to be equal to that across the plate, and having calculated the mass overlying the plate, we could then calculate the mean depth-averaged flow velocity across the plate,

$$\bar{u} = q/\sigma. \quad (11)$$

To extract the power spectral density of the flow's basal force, we processed data from the accelerometers using Kirchhoff-Love plate theory (Love & Darwin, 1888) and assuming perfect isolation of the plate from the channel and linear attenuation within the plate. On the basis of the steel's technical documentation (John Steel, 2019; Steel SS, 2019), we took its density to be $\rho_p = 7800 \text{ kg m}^{-3}$, its Young's modulus to be $E_p = 200 \text{ GPa}$, and its Poisson's ratio to be $\nu_p = 0.29$. Then, its bending stiffness was $D = E_p H^3 / 12(1 - \nu_p^2)$ and the mean gap between the resonant frequencies at which its motion was sensitive to forcing was $\Delta_f = 2\sqrt{D}/XY\sqrt{\rho_p H} \approx 400 \text{ Hz}$. Assuming that the spectral density of an impact's force varied little over this frequency scale, this spectral density was estimated using D , the proportion of the plate's energy \mathcal{P} in its steel structure's vertical displacements, the quality factor Q describing the attenuation of energy in the plate, and the accelerations $a_j(t)$ measured by the four accelerometers, as

$$P_F(f) = \frac{|\tilde{F}(f)|^2}{\Delta t} \approx \frac{(\rho_p H)^{3/2} XY \sqrt{D}}{\pi \mathcal{P} Q f \Delta t} \langle \sum_{j=1}^4 |\tilde{a}_j(f)|^2 \rangle_{\Delta f}, \quad (12)$$

where Fourier transforms are over a time interval $\Delta t = 0.2 \text{ s}$, and $\langle \cdot \rangle_{\Delta f}$ represents a moving average over frequency, with window width $\Delta f = 2 \text{ kHz}$. We describe in S7, section S7.1 the derivation of this relation and the calculation of $|\tilde{a}_j|^2$ from the voltage output of the accelerometers' conditioning amplifier; in section S7.2 the calibration we performed to measure the plate parameters $\mathcal{P} = 0.25$ and $Q = 99$ and to extend the flat frequency range of the accelerometers to 120 kHz; and in section S7.3 the validation of this work. The gaps between the plate's resonant frequencies limit both the resolution and the lower limit of our P_F -measurements to 1 kHz, whilst an accelerometer resonance at 125 kHz prevents measurement above 120 kHz. Measurements have a frequency-dependent, systematic relative error of typical magnitude around 40%, due to an imperfect attenuation model and variation in the number of resonant frequencies within each 2 kHz interval.

Finally, to extract profiles of kinematic properties at the channel wall, we analysed the images taken by the high-speed camera, using particle tracking velocimetry and Gaussian coarse-graining. Analysing each frame in turn, we detected the positions (x_j, z_j) of particles at the channel walls and, tracking particles between consecutive frames, calculated their mean velocities over each 0.5 ms interval. Calculating the smoothed velocities \mathbf{u}_j over five frames, or 2.5 ms, we estimated the downslope-averaged and time-averaged base-normal profiles at the channel's wall of relative vol-

ume fraction $\phi_w(z)$, mean velocity $\mathbf{u}_w(z)$, and granular temperature $T_w(z)$ as

$$\phi_w(z) = \langle \sum_j C(z_j; z) \pi d^2 / 4 \rangle_{\Delta t_c}, \quad (13)$$

$$\mathbf{u}_w(z) = \langle \sum_j C(z_j; z) \pi d^2 \mathbf{u}_j / 4 \rangle_{\Delta t_c} / \phi_w(z), \quad (14)$$

$$T_w(z) = \langle \sum_j C(z_j; z) \pi d^2 \|\mathbf{u}_j - \mathbf{u}_w(z)\|^2 / 4 \rangle_{\Delta t_c} / \phi_w(z), \quad (15)$$

where averages are over all frames recorded by the camera, sums are over all particles tracked in each frame, and C is a Gaussian weight function, localised around z and with integral over the total spatial domain equal to 1. This process is described in detail in section S8.

While the irregularity of the flow's base and surface complicate the definition of the flow thickness h , we take the base-normal co-ordinate z to be zero at the top of the base's fixed beads, and extract h as the value of z at which $\phi_w(z)$ drops below half its maximum value,

$$h = \min\{z > \operatorname{argmax} \phi_w | \phi_w(z) < \max(\phi_w)/2\}. \quad (16)$$

For a flow with constant particle volume fraction below a level surface, this exactly corresponds to the intuitive flow depth. Whilst other reasonable definitions lead to different values of h and of all quantities derived from it, they do not alter our conclusions.

2.3 Model Predictions

For each of the models described in section 1.2, for a granular flow's seismic signal, we inferred predictions for the experimental seismic signal. Specifically, we expressed a prediction \hat{P}_F for the power spectrum of the base-normal force applied by the flow to the instrumented plate, as a function of the flow properties specified in section 2.2: the mean depth-averaged flow velocity \bar{u} , the mass overburden per unit area σ , the flow depth h , and the channel-wall profiles $u_w(z)$ and $T_w(z)$ of downslope velocity and granular temperature. Since previous authors attempted to predict slightly different seismic properties and used slightly different flow properties, no directly applicable expressions are in the articles introducing the models (Kean et al., 2015; Lai et al., 2018; Farin, Tsai, et al., 2019; Bachelet, 2018). We therefore worked from equations (2) and (6); used the models' methods of estimating those equations' variables, as described in sections 1.2.1 and 1.2.2; and removed Green's functions as described in section 1.3, to predict the basal force's power spectrum rather than the power spectrum of a seismic station's response. Recalling that $g \cos \theta$ denotes base-normal gravitational acceleration, d the particles' mean diameter, and ρ their density, and approximating the flow area generating the measured signal by the instrumented plate's area $A = XY$ and the flow's mean volume fraction by $\phi = \sigma / \rho h$, these predictions could then be compared to the measured power spectra P_F .

The model introduced by Kean et al. (2015) predicts the seismic signal generated by a granular flow covering a certain area, using its surface velocity and the base-normal component of its weight per unit area. If the near-base velocity of the flow scales with its surface velocity, as Kean et al. (2015) suggests, then both will scale with the depth-averaged velocity \bar{u} , so to calculate predictions we estimated the velocity u of equation (2) with \bar{u} and the impulse Δp with $\sigma g \cos \theta$, the measured base-normal component of the flow's weight per unit area. We may therefore write the model's prediction for

P_F , for signal periods $1/f$ well above the duration of a typical impact, as

$$\hat{P}_F^0 = K A \bar{u} (\sigma g \cos \theta)^2 / d^3. \quad (17)$$

K is a free parameter, which in Kean et al. (2015)’s model is equal to the product of a constant volume fraction; a constant of proportionality between \bar{u} and the near-base flow velocity; and a squared constant of proportionality between the mean basal pressure and the typical impulse transferred by a basal impact. No indication is given as to its value, so it must be found by fitting.

In contrast, the model introduced by Lai et al. (2018) requires no free parameter. Noting that the experimental particles have a narrow diameter distribution, with 94th percentile approximately equal to its mean d , and using the appropriate substitutions for u and Δp in equation (2), the model’s prediction for P_F is the constant

$$\hat{P}_F^0 = \pi^2 \rho^2 A d^3 \bar{u}^3 / 9, \quad (18)$$

with the implicit assumption that the volume fraction is equal to 1. Again, this prediction is expected to be valid only for signal periods $1/f$ well above the duration of a typical impact.

The two models described by Farin, Tsai, et al. (2019) are developments of this model, with that article’s equation (16) developing the definition of the impulse denoted Δp in our equation (2). Within the same frequency range as in prior paragraphs, the associated predictions for $P_F(f)$ are the constants

$$\hat{P}_F^0 = \pi^2 \rho^2 \phi A d^3 (1 + e)^2 \xi(v) u_b^3 / 36, \quad (19)$$

where e is a constant coefficient of restitution; $\xi(v) \approx 0.053(1 + 5.6v^2)$ is a non-dimensional function accounting for variation in impacts’ geometry; and v and u_b define the velocities of base-impacting particles $u_b(\mathbf{e}_x + v\mathbf{e}_v)$, for randomly directed unit vector \mathbf{e}_v .

In the ‘thin-flow’ model, $u_b = \bar{u}$, whereas in the ‘thick-flow’ model $u_b = \chi \bar{u} d / h$ for velocity profile shape factor χ , assumed constant and between 1 and 1.5. The model-specific parameters are e , v and χ , which can neither be reliably measured in individual experiments nor individually determined via fitting. We therefore take $e = 0.9$, consistent with the rebound heights of particles dropped onto the instrumented plate; take $\chi = 1.25$, consistent with the velocity profiles measured at the channel’s wall and introducing an error factor of at most 2; and fit the free parameter v , corresponding to the normalised standard deviation of base-impacting particles’ velocities. Farin, Tsai, et al. (2019)’s derivation of ξ makes unphysical assumptions (e.g. that impacting particles’ velocities differ from $u_b \mathbf{e}_x$ by an exactly constant magnitude $v u_b$ and that, for each impact velocity, all possible impact locations are equally likely), so the best-fit value of v for an otherwise-accurate model will not exactly equal the true normalised standard deviation, but a model cannot be said to be accurate unless this best-fit value is a physically reasonable approximation. Specifically, the energy associated with velocity fluctuations is drawn from the mean flow and dissipated rapidly, so that we expect the typical magnitude of velocity fluctuations to be less than the mean velocity, and hence a condition for model accuracy is that $v < 1$.

To further assess the assumptions of the ‘thick-flow’ and ‘thin-flow’ models, we extended each model to higher frequencies. Farin, Tsai, et al. (2019) assumes binary, elastic, normal interactions during impacts, with impact velocities such that particle deformation in our experiments will be quasistatic and the Hertz theory described in S3 will apply. Applying this theory to the impact velocities and geometry assumed by Farin, Tsai, et al. (2019), we therefore compute predictions for P_F over a larger

frequency range than that considered by the original article, as

$$\hat{P}_F(f) = \frac{\int_{S^2} d^2 \mathbf{e}_v \int_{S_{\pi/6}^2} d^2 \mathbf{e}_n (u_n \mathbf{e}_n \cdot \mathbf{e}_z)^2 \zeta(\tau f) \mathcal{H}(u_n)}{\int_{S^2} d^2 \mathbf{e}_v \int_{S_{\pi/6}^2} d^2 \mathbf{e}_n (u_n \mathbf{e}_n \cdot \mathbf{e}_z)^2 \mathcal{H}(u_n)} \hat{P}_F^0 \quad (20)$$

for unit sphere S^2 ; unit spherical cap $S_{\pi/6}^2$ with maximum polar angle $\pi/6$; normal impact velocity $u_n = u_b(\mathbf{e}_x + v\mathbf{e}_v) \cdot \mathbf{e}_n$; impact timescale $\tau(u_n)$ as defined by equation (3); non-dimensional function ζ as introduced in equation (4); and Heaviside step function \mathcal{H} .

Finally, the model of Bachelet et al. already predicts P_F over a large frequency range. Substituting equations (7) into (6) and moving from the well-defined particle layers considered in the thesis to the continuous profiles measured in our experiments, the predicted power spectral density of the basal force is

$$\hat{P}_F(f) = \frac{4\pi}{9} \phi A \rho^2 d^3 \int_0^h u'_w(z) T_w(z) \zeta(\tau_w(z) f) e^{-\gamma z} dz, \quad (21)$$

where u'_w is the derivative of u_w with respect to z ; ζ is the non-dimensional function in equation (4); impact timescale $\tau_w(z)$ is defined with respect to $T_w(z)$ as τ_j is to T_j in equation (7); and constant γ is a free parameter, to be determined by fitting.

We compare these predictions to the measured power spectra P_F in section 3.3, but first we define the time period and the frequency-space properties used for the comparison, by considering the evolution of the flow (section 3.1) and the form of the power spectrum of the basal force (section 3.2).

3 Results

3.1 Evolution of the Flow

In each experiment, the flow passing a given point evolved through four stages that could be distinguished from measurements of outflow mass M and the net normal force on the plate F_z : I) precursory saltation of particles released at the start of the experiment; II) arrival of the dense flow's front; III) steady flow; and IV) decay of the flow. These corresponded to different signals measured at the instrumented plate, as illustrated for two different experiments in Figure 3.

As Figure 3 illustrates, saltating particles in stage I contributed little to the outflow mass M and to the net downslope and normal forces F_x and F_z , with an implied number density of around one particle per cm^2 of plate surface, but such particles applied basal forces with significant spectral density P_F across a wide frequency range. Similarly, the dense front's arrival in stage II had a short duration, but was associated with an intense, broad power spectrum of basal force, as high-velocity, surficial particles reached the front and impacted the plate. In general, as in Figure 3a, the power spectrum at high frequencies then dropped during stages III and IV, indicating that impact velocities in the dense flow's bulk were lower than those of high-velocity saltating particles. For 'transitional-regime' flows, however, P_F remained the same during stages II and III, as in Figure 3b, reflecting the continued saltation within each flow that defines this regime.

Such variation of signal properties between different experiments is summarised in Table 1. With increasing channel incline $\tan \theta$ and release gate height h_g , the duration of stage I decreased rapidly and that of stage II decreased slightly, as the speed of the dense flow front increased to the speed of saltating particles. Since the same changes greatly increased the high-frequency spectral density P_F of the plate-normal force during stage III, which had duration determined by the reservoir's capacity and

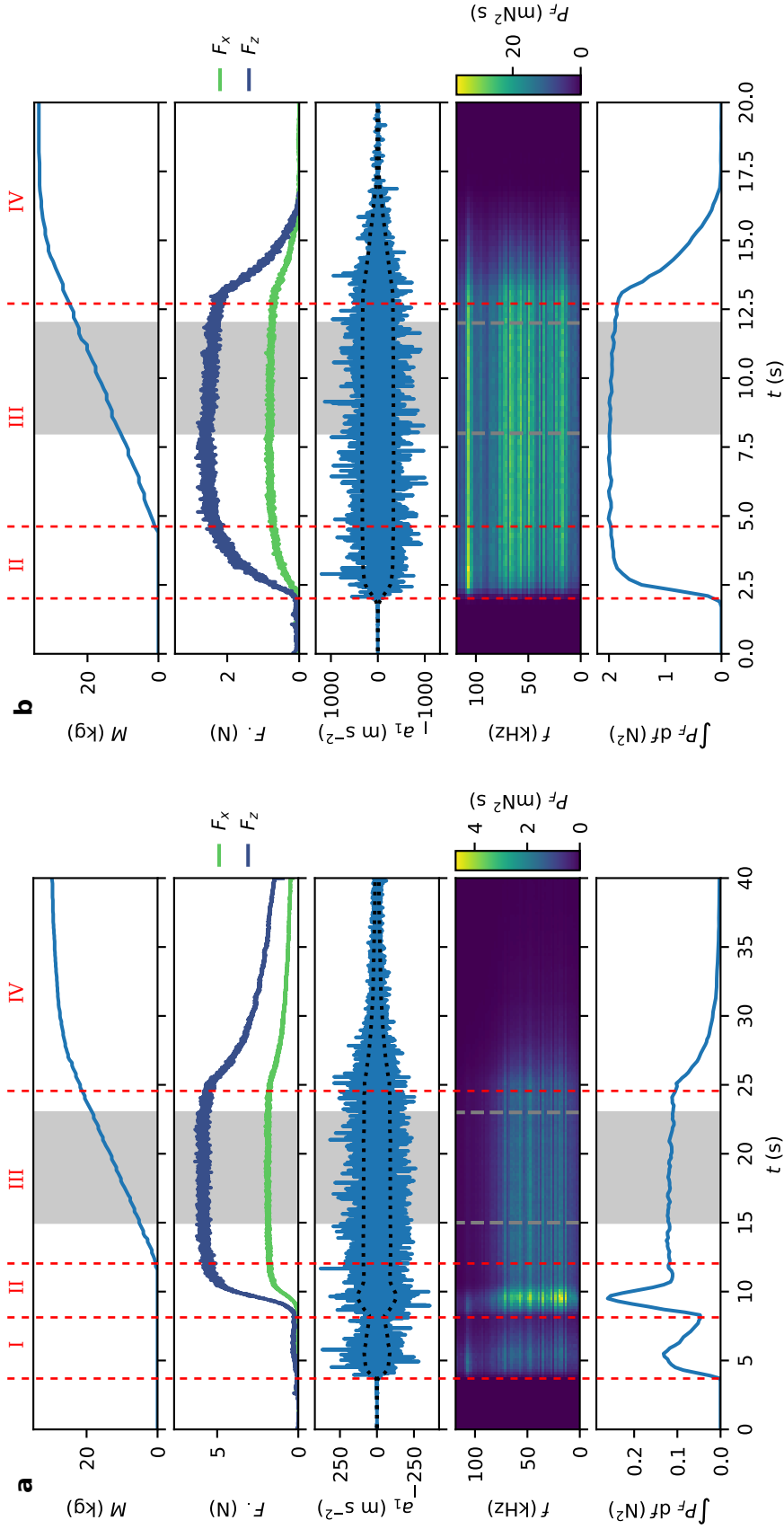


Figure 3. *Examples of flow properties' evolution over time.* Plots over time t of the cumulative outflow mass M ; the net downslope and normal forces F_x and F_z applied to the instrumented plate; a measured normal plate acceleration a_1 , with envelope indicated by dotted lines; the power spectral density P_F of the plate-normal basal force; and the integral of this power spectrum, which equation (41) shows to be proportional to the seismic power transmitted to the instrumented plate. a) A dense flow at a channel incline $\tan \theta = 0.44$ ($\theta = 23.7^\circ$), with a release gate height $h_g = 20$ mm. b) A transitional-regime flow, with $\tan \theta = 0.52$ ($\theta = 27.5^\circ$) and $h_g = 28$ mm. Flow stages I to IV are labelled, where present, and the shaded region indicates the period of steady flow recorded by the camera, $t_d < t < t_d + \Delta t_c$.

Table 1. *Properties of the flow’s stages of evolution.* F_z and P_F are as defined in section 2.2, while f_c is the frequency at which P_F drops to half its mean value pre-maximum. Arrows (\rightarrow) indicate ranges over time in an experiment, while hyphens ($-$) represent the ranges over different experiments. \bullet indicates the value for dense flows and \circ for transitional-regime flows, wherever they differed significantly.

Flow stage	I	II	III	IV
Durations (s)	0 – 40	2 – 8	4 – 150	5 – 20
F_z (N)	$O(0.1)$	$0 \rightarrow (1 - 10)$	1 – 10	$(1 - 10) \rightarrow (0 - 2)$
f_c (kHz)	> 100	> 90	$\bullet 70 - 110$ $\circ > 100$	$\bullet 70 - 110$ $\circ > 100$
$\int P_F df$ (N ²)	$O(0.1)$	0.02 – 2	0.003 – 3	$(0.003 - 3) \rightarrow 0$

decreasing with h_g , the contribution of stage I to the total generation of seismic energy decreased from around 70 % to less than 0.1 %, while the contribution of stage II remained between around 10 % and 20 %, and the contributions of stages III and IV increased. In contrast to this pattern of variation, the net normal force F_z increased with h_g but, for each h_g , decreased with increasing $\tan \theta$; the same h_g -determined flux of particles was maintained by faster flows, which were therefore thinner. These opposing trends indicate the independence of F_z and $P_F(f)$ for $f \neq 0$, with the former the mean force applied by the flow, and the latter associated with the force’s fluctuations about this mean.

In this article, we restrict our attention to stage III of the flow’s evolution, in which the flow’s steadiness ensured that all measurements were of the same flow state. Specifically, between different $\Delta t = 0.2$ s time intervals within the duration Δt_c of steady flow recorded by the camera, the per-second rate of change of outflow mass M had a standard deviation of around 10 % of its mean value, while the standard deviations of F_x and F_z were around 1 % and that for $\int P_F df$ around 5 %. Similarly, we examined the profiles of kinematic properties at the channel wall, averaged in turn over each decile of time $t_d + n\Delta t_c/10 < t < t_d + (n + 1)\Delta t_c/10$ within the period recorded by the camera. Within the flow, kinematic properties at the channel wall were steady over time, in the sense that the values of $\phi_w(z)$, $\mathbf{u}_w(z)$ and $T_w(z)$ varied by at most a few percent over time, for each z satisfying $\phi_w(z) > \max_z \phi_w(z)/2$.

3.2 Power Spectrum of the Basal Force

Averaging over this period of steady flow, by taking $\Delta t = \Delta t_c$ in equation (12), we calculated the power spectrum of the base-normal force applied by the flow to the plate and find it to be consistent with impacts of short duration. As in the example shown in Figure 4, the power spectral density $P_F(f)$ is approximately constant over a large frequency range and displays the same decay beyond a given corner frequency as Hertz theory predicts for a single impact. The high, $O(100 \text{ kHz})$ corner frequencies are comparable to those predicted by equation (3) for the small, $O(1 \text{ mm})$ experimental particles, while the deviations from power spectra proportional to equation (4) are consistent between experiments and generally consistent with the systematic errors discussed in section 2.2, as estimated in section S7.3.

We described the power spectrum by two quantities: its low-frequency amplitude P_F^0 and its corner frequency f_c . We calculated f_c as the frequency at which $P_F(f)$ drops to half its mean pre-maximum value, so that for errorless measurement of a Hertzian impact it would be equal to approximately $0.208/\tau$, for the impact timescale τ defined

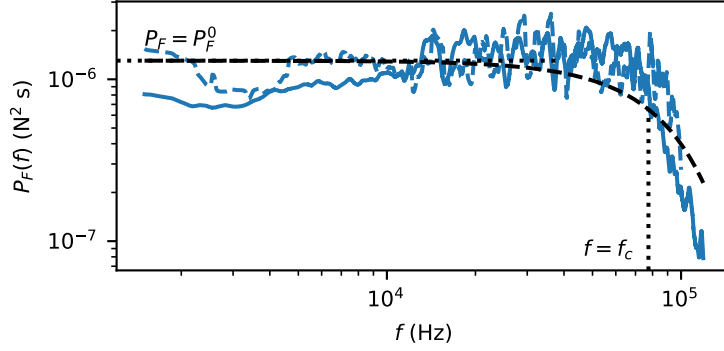


Figure 4. Example of the plate-normal force’s power spectral density during steady flow.

The measured power spectrum (blue, solid line) corresponds to the same experiment as Figure 3a, with channel incline $\tan \theta = 0.44$ ($\theta = 23.7^\circ$) and release gate height $h_g = 20$ mm. The dotted lines indicate the corner frequency $f_c = 77.5$ kHz and the low-frequency amplitude $P_F^0 = 1.29$ mN² s. The black dashed line indicates the Hertzian power spectrum fit to these values, closely approximating the functional form predicted by the model of Bachelet et al. and by our extensions of Farin, Tsai, et al. (2019)’s models. It was calculated from equations (3) and (4) and corresponds to 4,000 Hertzian impacts per second, each at normal velocity $u_n = 0.9$ m s⁻¹, of the $d = 2$ mm experimental particles on the plate’s surface. The blue dashed line represents a ‘corrected’ power spectrum, calculated with section S7.3’s estimate for the frequency-dependent systematic relative error.

by equation (3). The systematic errors in $P_F(f)$ will result in systematic error in f_c of order 20%, for which we’re unable to compensate with our uncertain error estimates.. However, our measurements of f_c were sufficiently robust that we calculated P_F^0 as the arithmetic mean value of P_F over all frequencies less than $f_c/2$, with systematic errors in P_F cancelling out over this range. We could then compare these experimentally measured values with the model predictions, computed as described in section 2.3.

3.3 Tests of Existing Models for Flows’ Seismic Signals

To assess the model predictions described in section 2.3, we compared their predictions \hat{P}_F^0 for the low-frequency value of the basal force’s power spectrum to the measured values P_F^0 . Where possible, we also inferred a prediction \hat{f}_c for the corner frequency of the basal force’s power spectrum, as the frequency at which $\hat{P}_F(f)$ dropped to half its maximum value, and we compared this prediction with the measured value f_c . Where a model had a free parameter, we used the parameter value that minimised the sum over all experiments of $\ln(P_F^0/\hat{P}_F^0)^2$, which was equivalent to minimising the typical logarithmic error or maximising the model likelihood under the assumption that measurements were log-normally distributed about their predicted values (see S9). Table 2 lists these best-fit parameter values and Figure 5 shows the results of the comparisons.

The model introduced by Kean et al. (2015) predicts P_F^0 poorly, due largely to its incorrect assumption of proportionality between the pressure fluctuations relevant to P_F^0 and the mean pressure $\sigma g \cos \theta$ used as input. To best fit the measurements, the free parameter K had to take a value of 4.0×10^{-16} m⁴s², entirely unpredicted by the model, and even then predictions often differed from measurements by an order of magnitude (Figure 5a). Notably, the model’s predictions \hat{P}_F^0 decrease for flows at

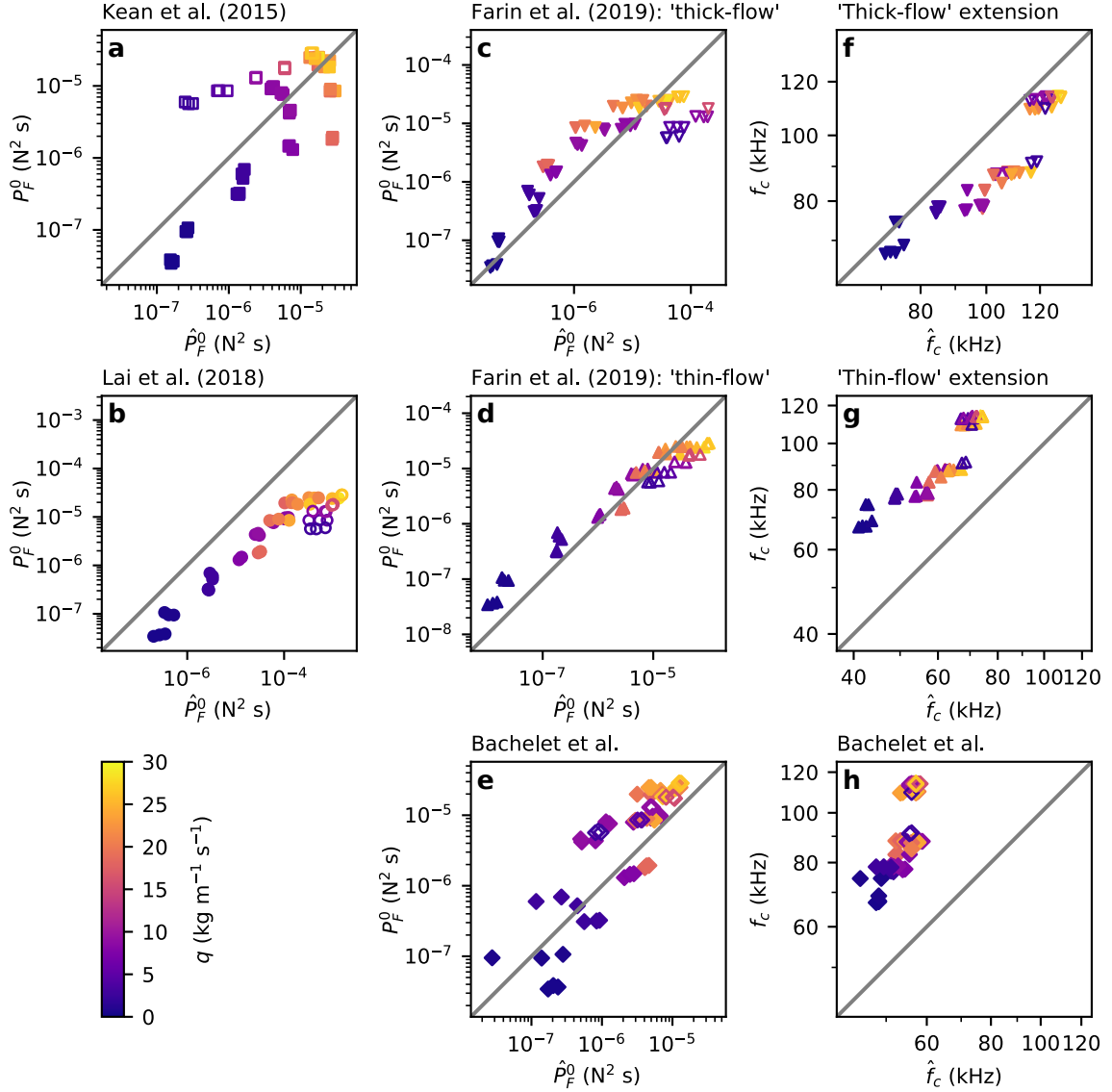


Figure 5. Comparison between models' predictions (x-axes) and experimental measurements (y-axes) for the basal force's power spectrum during steady flow. Plots f, g, and h represent predictions for the corner frequency of the basal force's power spectrum, while all others represent predictions for the power spectral density's value at frequencies well below this corner frequency. In all plots, the grey line represents perfect agreement between predictions and measurements, colours indicate each experiment's mass flux q per unit channel width, and unfilled symbols represent experiments for which the flow was in the transitional regime.

Table 2. *Summary of model testing.* For each of the existing models described in section 1.2, we list the flow measurements defined in section 2.2 that are required to predict the flow’s high-frequency seismic signal. We further record the equation for predictions \hat{P}_F^0 ; the free parameter value for which such predictions best fit measurements; and the geometric standard error $\epsilon = \exp \left[\sqrt{\frac{1}{N} \sum \ln(P_F^0/\hat{P}_F^0)^2} \right]$ of these predictions.

Model	Inputs	Equation	Best-fit parameter	ϵ
Kean et al. (2015)	\bar{u}, σ, θ	(17)	$K = 4.0 \times 10^{-16} \text{ m}^4 \text{ s}^2$	4.2
Lai et al. (2018)	\bar{u}	(18)	n/a	18.5
Farin, Tsai, et al. (2019)	\bar{u}, σ, h	(19)		
‘thick-flow’			$v = 9.8$	3.2
‘thin-flow’			$v = 0.51$	2.1
Bachelet et al.	σ, h, u_w, T_w	(21)	$\gamma = 0 \text{ m}^{-1}$	3.9

higher channel inclinations or in the transitional regime, for which the mean pressure is lower, whereas such flows’ higher impact energies in fact resulted in higher pressure fluctuations and so larger measured values P_F^0 .

In contrast, the model introduced by Lai et al. (2018) accurately predicted variation in P_F^0 between experiments, with predictions for dense flows consistently 3 to 10 times larger than the measured values (Figure 5b). For transitional-regime flows, the predictions’ errors are larger, due to the model’s implicit assumption that the volume fraction is equal to one.

Of the two models described by Farin, Tsai, et al. (2019), the model derived for flows thicker than the largest particles is less accurate than that derived for thin flows, with the former’s fit to observations requiring an unrealistically large ratio v between the magnitudes of velocity fluctuations and of the mean velocity. As explained in section 2.3, realism demands that $v < 1$, but the ‘thick-flow’ model requires $v = 9.8$ for predictions \hat{P}_F^0 to be as large as measurements P_F^0 and, in that case, the predictions are too large for the transitional-regime flows (Figure 5c). For the ‘thin-flow’ model, meanwhile, the best-fit value is $v = 0.51$, which is physically reasonable and provides an excellent fit of \hat{P}_F^0 to P_F^0 over all experiments (Figure 5d).

This difference between the ‘thick-flow’ and ‘thin-flow’ models’ best-fit values of v is reflected in the predictions \hat{f}_c they implied for the corner frequency of the basal force’s power spectrum, calculated according to our extensions of these models using equation (20). The higher v required for the ‘thick-flow’ model results in higher predictions \hat{f}_c , matching the measured values f_c (Figure 5f), whereas for the ‘thin-flow’ model predictions are consistently approximately 30 % smaller than the measured values (Figure 5g). Predicted corner frequencies \hat{f}_c are as large as measurements f_c only for typical impact velocities six times larger than the flows’ mean velocities, suggesting that our measurements f_c were slight, but systematic, overestimates. Such systematic disagreement is consistent with the systematic errors in P_F discussed in sections 2.2 and 3.2, or with 30% error in the particle properties in equation (3).

Finally, the predictions of the ‘Bachelet et al.’ model followed the correct trend but had a wide dispersion (Figure 5e). The free parameter γ , representing signal attenuation within the flow, had best-fit value 0, indicating that the unattenuated contributions of all synthetic impacts are necessary for \hat{P}_F^0 to be large enough to compare to P_F^0 . Even then, the lower energies of synthetic impacts are reflected in

predictions \hat{f}_c for the power spectrum’s corner frequency that are even lower than those of our extension to Farin, Tsai, et al. (2019)’s ‘thin-flow’ model (see Figure 5h).

Overall, of the five models, the ‘thin-flow’ model described in Farin, Tsai, et al. (2019) best fits the results from our experiments. While the fit is imperfect, the predictions \hat{P}_F^0 of this model differ from the measured values P_F^0 by a typical factor of 2.1, lower than that for the other models, and the model’s accuracy is approximately equal across the entire range of experiments, including for the flows in the transitional regime. Constructing a statistical model for each physical model, by assuming $\ln P_F^0$ was normally distributed about $\ln \hat{P}_F^0$ with constant variance, the ‘thin-flow’ model is also the preferred model by the Akaike information criterion (see S9), indicating that its additional free parameter compared to the Lai et al. (2018) model is worthwhile in an information theoretic sense. This analysis did not compare models’ predictions to the measured corner frequencies f_c , due to the likelihood of systematic error in the latter, but our extensions to the models of Farin, Tsai, et al. (2019) both predicted a trend in \hat{f}_c consistent with measurements.

4 Discussion

4.1 Velocity Profiles and the ‘Thin-flow’ Model

That the ‘thin-flow’ model best predicts the experimental results is surprising, because we do not expect the velocity profile within the flow to be consistent with the model’s assumptions. The ‘thin-flow’ model assumes that particles at the flow’s base move across the instrumented plate’s surface at approximately the flow’s mean velocity, whereas previous authors suggest that the plate’s roughened surface should impose a no-slip condition on the flow, in the sense that particles’ velocities should tend to zero towards the flow’s base (GDR MiDi, 2004; Jing et al., 2016). Furthermore, as the example of Figure 6 demonstrates, the velocity profiles we observe at the channel’s wall are consistent with this no-slip condition (which we note is distinct from any micromechanical condition on rolling or sliding at particle contacts).

We propose two possible explanations for the success of the ‘thin-flow’ model. The first is that the instrumented plate’s flow-induced vibration reduces the effective friction between it and the flow, leading to basal slip and a basal flow velocity closer to the flow’s mean velocity. The second is that basal particles have low velocities, but that impacts away from the flow’s base make significant contributions to the basal force exerted by the flow, in such a way that the total contribution of these impacts scales with the mean velocity of the flow.

The first explanation is supported by the literature on frictional weakening and by measurements of the plate’s effective friction coefficient with the flow. The reduction by vibration of a granular medium’s effective friction has been documented in discrete element simulations (e.g. Capozza et al., 2009; Ferdowsi et al., 2014; Lemrich et al., 2017) and experiments (e.g. Johnson et al., 2008; Dijksman et al., 2011; Lastakowski et al., 2015; Léopoldès et al., 2020), with suggestions for the necessary vibration amplitude being a particle strain of order 10^{-6} (Ferdowsi et al., 2014), a velocity of order $100 \mu\text{m s}^{-1}$ (Lastakowski et al., 2015), and an acceleration of order $0.1g$ (Dijksman et al., 2011). Even in the experiments in which the plate vibration amplitudes during steady flow were lowest, the plate had approximate root mean square normal displacement 10 nm , velocity $100 \mu\text{m s}^{-1}$, and acceleration 20 ms^{-2} (around an order of magnitude larger than were measured away from the plate), so a vibration-induced reduction in friction appears viable. Furthermore, the effective friction coefficients μ that we measure between the plate and the flow are too low to prevent basal slip on the surface of the plate, with Figure 7a showing that $\mu < \tan \theta$ for all channel inclines

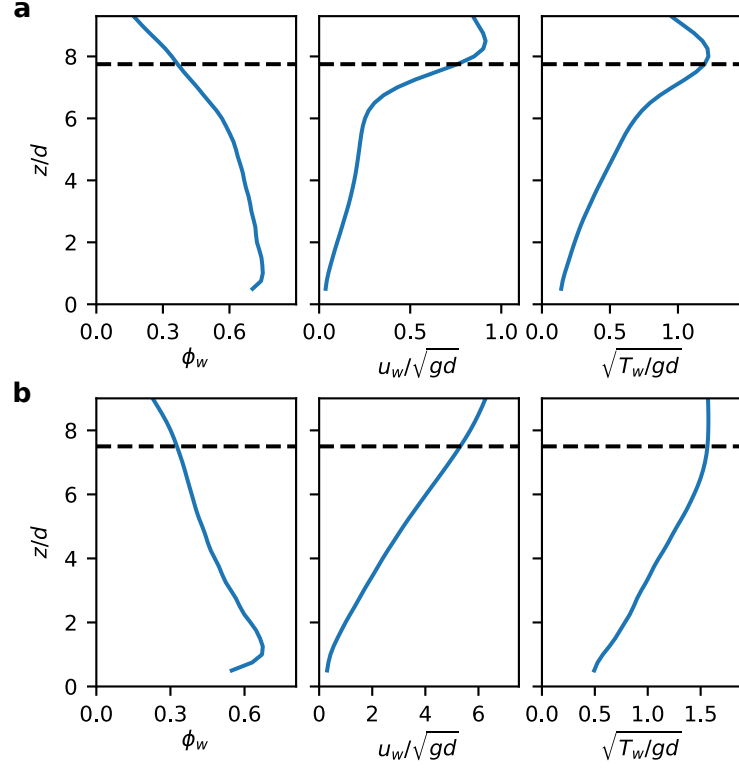


Figure 6. *Examples of kinematic properties' steady profiles at the channel wall.* Profiles are estimates from particle tracking velocimetry of the relative volume fraction ϕ_w , the downslope velocity u_w , and the square root $\sqrt{T_w}$ of the granular temperature, non-dimensionalised by $\sqrt{gd} = 0.14$, while the dashed lines represent the flow thicknesses h inferred from the profile of ϕ_w . Profiles are taken from the same experiments as for Figure 3: a) a dense flow at channel incline $\tan \theta = 0.44$ ($\theta = 23.7^\circ$) with release gate height $h_g = 20$ mm; and b) a transitional-regime flow at channel incline $\tan \theta = 0.52$ ($\theta = 27.5^\circ$) with release gate height $h_g = 28$ mm.

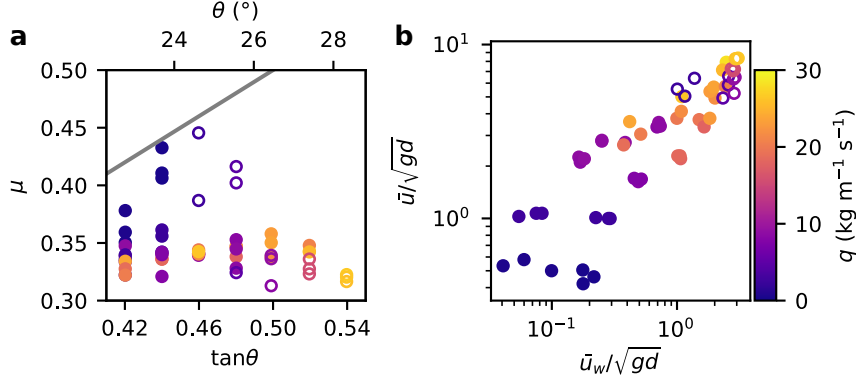


Figure 7. *Complications in modelling the granular flow.* a) Measurements of the effective friction coefficient μ between the instrumented plate and the flow fall consistently below the condition $\mu = \tan \theta$ for zero basal slip (grey line). b) The depth-averaged particle velocity measured at the channel wall \bar{u}_w is poorly correlated with the mean velocity \bar{u} calculated from bulk flow properties. Colours indicate each experiment’s mass flux q per unit channel width, and unfilled symbols represent experiments for which the flow was in the transitional regime.

$\tan \theta$. This implies that basal particles accelerate across the plate’s surface, towards the flow’s mean velocity.

On the other hand, we do not directly measure any increases in velocity associated with basal slip. Over the 8 cm distance downslope captured by the high-speed camera, averaging over each flow’s depth and each 4 cm half-window, the mean downslope velocities measured at the sidewall are uniform to within 10%. Away from the sidewalls, Tsang et al. (2019) suggests that a granular flow will adjust to a change in basal boundary conditions over a lengthscale of order \bar{u}^2/g , for mean flow velocity \bar{u} and gravitational acceleration g . This lengthscale varies in our experiments from 0.5 mm to 0.1 m, so that we would expect the effects of any basal slip to become evident at the flow’s surface within the length of the instrumented plate. However, having conducted particle image velocimetry with images captured by an overhead camera, for a flow at a channel incline $\tan \theta = 0.46$ ($\theta = 24.7^\circ$) and with release gate height $h_g = 20$ mm, we were unable to distinguish whether the flow’s surface’s slight acceleration across the plate was induced by the plate, or was simply a continuation of the flow’s acceleration towards a uniform state. Similarly, we attempted to detect changes in the velocity of basal particles, via Jop et al. (2005)’s method of examining soot erosion from an inserted metal plate, but our attempts were frustrated by the energetic particles’ rapid erosion of soot during the insertion and removal of the plate.

Consequently, the second explanation remains feasible, with good reasons why the model of Bachelet (2018) and Bachelet et al. (2021), despite being derived to describe the contributions of impacts throughout the flow’s depth, might describe such contributions less well than the ‘thin-flow’ model. Firstly, the model of Bachelet et al. uses profiles u_w and T_w that are measured at the channel’s wall and may not be representative of those in the flow’s interior. In fact, the mean particle velocity measured at the channel wall \bar{u}_w correlates poorly with the mean velocity \bar{u} calculated with equation (11) (see Figure 7b), while the monotonically increasing profiles $T_w(z)$ differ from the S-shaped profiles that previous authors propose for granular temperature profiles in the flow’s interior (Hanes & Walton, 2000; Silbert et al., 2001; Gollin et al., 2017). Secondly, Bachelet et al. may suggest an incorrect dependence of the seismic signal on these profiles, with a particularly strong assumption being that

of a frequency-independent attenuation constant γ . We were unable to dramatically improve the predictions of Bachelet et al.’s model by modifying its inputs, e.g. by multiplying the profiles $u_w(z)$ and $\sqrt{T_w(z)}$ by \bar{u}/\bar{u}_w , but, under a different model for the contributions of impacts throughout the flow, such contributions could explain the relationship observed between the mean velocity \bar{u} and the basal force’s power spectrum P_F .

To test which explanation accounts for the success of the ‘thin-flow’ model, we suggest that our experimental conditions be replicated with discrete element simulations. In such simulations, a suitably roughened base could be fixed in position to prevent any vibration-induced reduction of its effective friction coefficient and any basal slip, as records of base-adjacent particles’ velocities could verify. If the ‘thin-flow’ model continued to be accurate, then the first, ‘basal slip’ explanation would be disproven. Records of particle velocities throughout the flow would then permit variants of Bachelet et al.’s model to be tested and their assumptions examined, using base-normal profiles of velocity and granular temperature measured within the flow’s bulk rather than at its edge, to explain and improve on the ‘thin-flow’ model’s accuracy. If the ‘thin-flow’ model were no longer accurate, however, then our first explanation would be proven and the model shown to apply only to flows with basal slip. The recorded particle velocities would then permit development of a different model, by which a small number of flow parameters could predict the seismic signal generated by flows without basal slip, analogous to the use of \bar{u} in the ‘thin-flow’ model, or of the inertial number to predict a dense granular flow’s kinematic properties.

4.2 The Inertial Number and the Seismic Signal

For given grains, the argument of e.g. da Cruz et al. (2005), that all local, non-dimensional flow parameters should be functions of the local inertial number I , applies as much to the fluctuating forces exerted by a flow as to the flow’s kinematic properties. This ‘ $\mu(I)$ ’ framework will not apply where a) the flow’s rheology is ‘non-local’, in the sense that the internal stress depends on derivatives of the strain rate rather than on only the strain rate’s local value (Clark & Dijkstra, 2020), or b) particles are sufficiently agitated that kinetic theory describes their motion better than a mean shear rate (Goldhirsch, 2003), but we can use the framework to discuss our results in the context of Hsu et al. (2014)’s and Taylor and Brodsky (2017)’s.

If the ‘ $\mu(I)$ ’ framework applies within a two-dimensional, steady, fully developed shear flow above a plate with incline $\tan \theta$, a macroscopic force balance implies that I is constant and can be estimated from bulk measurements of the flow’s mean velocity \bar{u} , volume fraction ϕ , and depth h (Jop et al., 2005), as

$$\hat{I} = \frac{5\bar{u}d}{2h\sqrt{\phi g h \cos \theta}}. \quad (22)$$

Even if our experimental flows were fully developed, without basal slip, the local inertial numbers within them will have differed significantly from \hat{I} . Non-locality will have been particularly significant within slow, thin flows; particles will have been particularly agitated within transitional-regime flows; and friction at the channel’s walls will have altered the force balance (Fernández-Nieto et al., 2018). We nevertheless calculated \hat{I} as a descriptor for each flow, with $\phi = \sigma/\rho h$ for flow mass per unit area σ and particle density ρ and with other quantities defined in sections 2.1 and 2.2. We see in Figure 8a that the ‘ $\mu(I)$ ’ framework applies for the dense experimental flows, insofar as the local, non-dimensional parameter $\tan \theta$ is closely related to \hat{I} .

To examine the relevance to each flow’s seismic signal of this inertial number estimate \hat{I} , we define a non-dimensional parameter $\delta\mathcal{F}^2$ expressing the mean squared magnitude of high-frequency basal force fluctuations on the instrumented plate, nor-

malised by the mean basal force. From the low-frequency amplitude P_F^0 and corner frequency f_c of the basal force’s power spectrum, and from gravitational acceleration g , inclination angle θ , plate length X and width Y , and measured mass overburden σ , we calculate for each flow

$$\delta\mathcal{F}^2 = \frac{2P_F^0 f_c}{(XYg\sigma \cos \theta)^2}. \quad (23)$$

To understand this definition, we recall from equation (8) that $XYg\sigma \cos \theta$ is the mean normal force applied by the flow to the instrumented plate, over the time interval Δt_c of steady flow recorded by the camera. Meanwhile, as Figure 4 indicates, $2P_F^0 f_c$ approximates the integral of the symmetric power spectral density $P_F(f)$ over all f with $|f| > 1$ kHz, this being the lowest frequency accessible to our measurements. Recalling that $\tilde{F}(f)$ is the Fourier transform over Δt_c of the normal force applied to the plate, $P_F(f) = |\tilde{F}(f)|^2 / \Delta t_c$. Combining these links and then applying the Plancherel theorem (Plancherel & Mittag-Leffler, 1910) to move to the time domain,

$$2P_F^0 f_c \approx \frac{1}{\Delta t_c} \int_{|f| > 1 \text{ kHz}} |\tilde{F}(f)|^2 df = \frac{1}{\Delta t_c} \int_{\Delta t_c} |\delta F(t)|^2 dt, \quad (24)$$

where δF is the fluctuating normal force on the plate, high-pass-filtered above 1 kHz. Assuming that pressure fluctuations are spatially uncorrelated on the lengthscale of the plate, as discussed in S2, $2P_F^0 f_c$ will be proportional to the plate’s area XY and $\delta\mathcal{F}^2$ to $1/XY$, but $\delta\mathcal{F}^2$ can be thought of as a rescaling by d^2/XY of a local flow parameter, for mean particle diameter d . Systematic errors in f_c will lead to error in $\delta\mathcal{F}^2$, but this error will be systematic and of negligible magnitude compared to $\delta\mathcal{F}^2$ ’s range of variation.

Plotting $\delta\mathcal{F}^2$ against \hat{I} for each flow, in Figure 8b, we see that this measure of the high-frequency seismic signal is strongly correlated with the estimated inertial number. This relationship between non-dimensional, local flow parameters is in accord with the ‘ $\mu(I)$ ’ framework, with more energetic flows producing more energetic seismic signals, even for flows to which the ‘ $\mu(I)$ ’ framework is otherwise inapplicable.

Comparing the relation of $\delta\mathcal{F}^2$ and \hat{I} to the relations proposed by previous authors, our results agree more closely with Hsu et al. (2014) than with Taylor and Brodsky (2017). Hsu et al. (2014)’s measurements aren’t equivalent to ours, but suggest the empirical scaling $\delta\mathcal{F}^2 \sim \hat{I}^{2.0}$, which is a reasonable first approximation to our results and closer than the $\delta\mathcal{F}^2 \sim \hat{I}$ relationship suggested by Taylor and Brodsky (2017)’s observation of direct proportionality between mean squared seismic accelerations and the inertial number. However, it is impossible to make a direct comparison without knowing the frequency dependence of the Green’s function relating the accelerations discussed by Taylor and Brodsky (2017) to the forces imposed by that article’s shear flow, while any inconsistency may be due to Taylor and Brodsky (2017)’s different procedure for estimating the inertial number. Differently estimated inertial numbers are likely to be even more inconsistent in geophysical contexts, so any $\delta\mathcal{F}^2(\hat{I})$ relation will be harder to apply to geophysical flows than our results in section 3.

4.3 The Application of Our Results to Geophysical Flows

Our results concern the fluctuating forces exerted by laboratory granular flows upon the base on which they travel, so their application to landquake signals necessitates consideration of two things: the Green’s function that determines a flow’s seismic signal from the forces it exerts, and the differences between geophysical flows’ forces and those that we’ve studied. We limit ourselves to describing the importance of an accurate Green’s function, rather than defining one, and to discussing the adjustments involved in moving from laboratory to geophysical flows, rather than validating them,

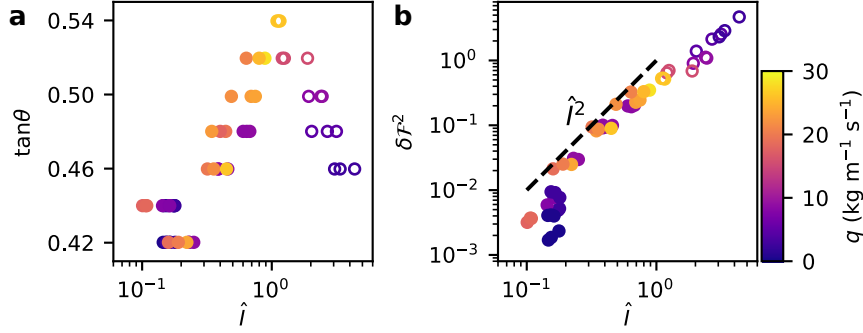


Figure 8. Relations between the inertial number \hat{I} estimated from bulk flow parameters and a) the channel incline $\tan\theta$, b) the normalised mean squared fluctuating force on the plate $\delta\mathcal{F}^2$. Colours indicate each experiment’s mass flux q per unit channel width, and unfilled symbols represent experiments for which the flow was in the transitional regime.

but we nevertheless propose tentative links between our results and the empirical relationships observed by previous authors.

4.3.1 The Importance of an Accurate Green’s Function

The forces exerted by a geophysical flow determine a measurable seismic signal only via a Green’s function, so an accurate Green’s function is necessary to interpret any landquake signal. Even the rate of seismic energy emission, which previous authors have used to describe geophysical flows directly, depends on the response of a flow’s base to the forces exerted upon it and hence on the Green’s function as well as the flow. This particularly complicates comparisons such as those of Farin et al. (2018), Farin, Mangeney, et al. (2019), and Bachelet et al. (2021), between the seismic energy emitted by geophysical flows and by experimental flows.

Even when different landquake signals are associated with the same Green’s function, the signals’ relative amplitudes depend on the frequency-dependence of that Green’s function, rather than on just the relative magnitudes of the forces exerted by the corresponding flows. Consequently, Green’s functions should be considered when assessing landslides’ relative magnitudes from their signals’ relative amplitudes, as in e.g. Norris (1994). We illustrate the Green’s function’s effect on seismic energy emission and signals’ relative magnitudes, using our experimental data, in S10.

Calculation of Green’s functions will be significantly more difficult for geophysical flows than for our laboratory-scale flows, especially since such functions will vary over time, as a flow propagates downslope, and over a flow’s spatial extent at any given time, as the forces exerted by different regions of the flow contribute differently to the signal at a given receiver. However, Allstadt et al. (2020) demonstrates that empirical Green’s functions can be used to successfully infer the forces exerted by flows from the seismic signals they generate, and shows that a debris flow’s unsaturated, coarse-grained front exerts rapidly fluctuating forces of much greater amplitude than those exerted by its fine-grained, saturated tail. This agrees with previous predictions (Lai et al., 2018; Farin, Tsai, et al., 2019) and suggests that, in the far field, the coarse-grained front’s contribution will dominate the seismic signal.

4.3.2 Adjustments to Forces for Geophysical Flows

That debris flows' coarse-grained fronts are so significant in landquake generation indicates the applicability of our results to such flows, as well as to entirely dry rock-slides and avalanches, whenever a granular flow's conditions match those of our dense and partially dense experimental flows. The circumstances under which this is true require investigation, but we believe broad applicability to be feasible. This is true whether or not our flows exhibit the vibration-induced basal slip discussed in section 4.1, since geophysical flows will experience basal slip whenever the friction coefficient of their base falls below its incline, and vibration-induced frictional weakening has been proposed as an explanation for geophysical flows' long runouts (Davies, 1982; Lucas et al., 2014). However, the application of our results to geophysical flows involves significant adjustments, firstly to the sizes of the flow and its constituent particles and secondly to the flow's evolution.

Clearly, geophysical flows of interest will be more extensive than our experimental flows and will involve larger particles, but these changes will not alter the underlying physics and simply necessitate adjustment of the values of flow area A and particle diameter d in the models of section 2.3. According to these models, a flow identical to those in our experiments, except with particles of radius 1 m, should produce a seismic force signal with power spectral density per unit flow area $\dot{P}_F(f)/A$, of order $(10^2 \text{ to } 10^6) \text{ N}^2 \text{ m}^{-2} \text{ s}$ below a corner frequency f_c of order 100 Hz. A more difficult adjustment is required to account for the wide particle polydispersity typical of geophysical flows (Takahashi, 1981; Nishiguchi et al., 2012), which makes d hard to define and necessitates consideration of the segregation of particles by size that is well-documented within granular flows (e.g. Garve, 1925; Gray, 2018). Farin, Tsai, et al. (2019) proposes a promising approach for each given model, of dividing the flow into a coarse-grained front and a fine-grained tail and calculating for each a percentile of the particle size distribution that will be representative, but this proposal requires validation.

Other necessary changes relate to the flow evolution, stemming from differences in particles' coefficient of restitution and in the mechanism of their release. The glass beads in our experiments underwent collisions more elastic than are typical in geophysical flows (Kim et al., 2015), resulting in our observations of sustained saltation at relatively low channel inclinations. This implies that the intense precursory saltation of flow stage I, discussed in section 3.1, is unlikely to be significant for most geophysical flows, though it may be analogous to rock falls at high slope inclinations. Similarly, the energetic, saltating particles observed in the steady stage III of transitional-regime flows are likely to be rare in geophysical flows, though the coexistence of a dense core and a saltating layer is documented in snow avalanches (Pudasaini & Hutter, 2006).

In fact, the entirety of the experimental flows' stage III is atypical of geophysical flows, since particles were released from the experimental reservoir over a long period at a constant flux, whilst the release of geophysical flows is rarely so steady or protracted. Therefore, our results should only apply to individual stages and regions of an unsteady and spatially varying geophysical flow, over each of which mean flow properties will be representative and related to the local forces exerted on the flow's base. The very front of a flow will resemble stage II of our experimental flows more than the stage III that we've studied in detail, and determination of quantities that are representative of an entire flow requires further work.

4.3.3 Comparisons with Empirical Results

Nevertheless, we can tentatively link our measurements of experimental flows' forces to the landquake signals of geophysical flows, by assuming the validity both of certain adjustments to those forces and of certain restrictions to the Green's function

linking geophysical forces to landquake signals. Firstly, we assume that any precursory saltation of a geophysical flow contributes so insignificantly to the signal as to be negligible and that our results apply to a flow area A whose contribution dominates the high-frequency signal. Secondly, we suppose that the release mechanism and size distribution of geophysical particles significantly affect the signal only by determining the flow's duration and a representative diameter of its particles. Thirdly, we assume that the signal's Green's function is constant over time and corresponds to transmission along a single wave path, without significant dispersion in time. Finally, we consider the signals only at frequencies lower than any force's power spectrum's corner frequency f_c , but high enough for the stochastic impact framework and hence our results to apply.

Under these assumptions, the landquake signal v_r between times t_r and $t_r + \Delta t$ will only depend significantly on the forces exerted by the landslide between times t_s and $t_s + \Delta t$, for some source-receiver delay $t_r - t_s$. Neglecting non-normal components, these forces will have a power spectral density within the relevant frequency band that is equivalent to those that we have studied and is well-described by the constant prediction \hat{P}_F^0 of Farin, Tsai, et al. (2019)'s 'thin-flow' model, for flow properties averaged between t_s and $t_s + \Delta t$. Writing $\tilde{G}(f)$ for the relevant frequency-space Green's function and f_0 and f_1 for the minimum and maximum frequencies under consideration, the mean squared amplitude of the signal will be

$$\langle v_r^2 \rangle_{\Delta t} = \frac{2}{\Delta t} \int_{f_0}^{f_1} |\tilde{v}_r(f)|^2 df \approx 2\hat{P}_F^0 \int_{f_0}^{f_1} |\tilde{G}(f)|^2 df. \quad (25)$$

Given this link, we can compare our results to the empirical relations discussed in section 1.1. Qualitatively, the landquake signal's envelope will have the same shape as the envelope of the time-retarded geophysical force, as Figure 3 shows to be the case for our experimental forces and acceleration signals. Adjusting these envelopes by excluding the precursory saltation and shortening the artificially prolonged stage of steady flow, our results therefore predict the distinctive 'spindle-shaped' signal envelopes associated with geophysical granular flows (Suriñach et al., 2005). Quantitatively, our results suggest that a flow's duration will equal its signal's, as in the empirical observations of e.g. Deparis et al. (2008), though our experiments are unlike those of Farin et al. (2018) in that our release mechanism prevents comparison with the observed empirical relationship between potential energy loss and signal duration. Similarly, we cannot follow Farin, Mangeney, et al. (2019) in comparing our results to the observations of e.g. Norris (1994), that the flow volume is correlated with the signal amplitude.

However, we can compare our results with other empirical relationships for the signal amplitude. Substituting equation (19) for \hat{P}_F^0 into equation (25) and assuming both constant particle properties and a constant Green's function, our results suggest that a flow of area A in which the particle volume fraction is ϕ and the mean flow velocity is \bar{u} will generate a signal with mean squared amplitude proportional to $\phi A \bar{u}^3$. Rearranging equation (22) for flow depth h and noting that the mean flow momentum per unit area $q = \rho \phi h \bar{u}$, for particle density ρ , we recover that

$$q^3 = \frac{25\rho^3\phi^2d^2\bar{u}^5}{4\hat{I}^2g\cos\theta} \text{ and } \bar{u}^3 = \left(\frac{4\hat{I}^2gq^3\cos\theta}{25\rho^3\phi^2d^2} \right)^{3/5}, \quad (26)$$

for bulk inertial number \hat{I} , representative particle diameter d , gravitational acceleration g , and slope angle θ . Among flows with constant \hat{I} and ϕ , the resulting landquake signals will therefore have root mean squared amplitude

$$v_{rms} \propto A^{1/2} q^{9/10} \cos^{3/10} \theta. \quad (27)$$

Whilst the assumption of constant \hat{I} is very strong, this quantity is close to those found empirically to be approximately proportional to landquake signal amplitude: the work rate against friction used by e.g. Schneider et al. (2010), which will be equal to $\mu Aq \cos \theta$ for basal friction coefficient μ , and the total flow momentum used by e.g. Hibert et al. (2015), equal to Aq . Holding all else constant, the scalings $A^{1/2}$ and A correspond to spatially separated impacts' signals being perfectly uncorrelated and perfectly correlated, respectively, so S2 suggests that $A^{1/2}$ is likely to be a better approximation, while the scalings $q^{9/10}$ and q are unlikely to be distinguishable in the field.

5 Conclusion

In conclusion, our experimental apparatus and data analysis permitted us to study the normal force exerted by a granular flow upon the base over which it travels, by measuring its high-frequency power spectral density and testing a range of existing models that predict this spectral density from the flow's properties. Figure 5 shows the 'thin-flow' model of Farin, Tsai, et al. (2019) to best predict the spectral density at frequencies well below its corner frequency and demonstrates that our extension of that model to higher frequencies, using Hertz theory, systematically underestimates the corner frequency by 30%. We've proposed that the success of the 'thin-flow' model, despite our experimental flows' thickness compared to their constituent particles, can be explained either by slip at each flow's base or by the contributions to the seismic signal of impacts throughout each flow's depth, and we've discussed the adjustments required to apply our results to the landquake signals generated by the forces of geophysical granular flows. Making such adjustments, under certain restrictive assumptions, the 'thin-flow' model's predictions are consistent with the empirical observation that a landquake signal's amplitude is approximately proportional to the momentum per unit area of the flow region that generated it.

Finally, our results are also relevant to two open questions on geophysical granular flows' dynamics: 1) the relation between the mean and fluctuating forces exerted by a flow; and 2) the low values of effective friction inferred for many geophysical flows. On the first question, previous authors have suggested that the typical magnitude of fluctuations is proportional to the magnitude of the mean force (McCoy et al., 2013; Hsu et al., 2014), but we show in Figure 8b that the ratio between the two, $\delta\mathcal{F}$, varies over two orders of magnitude between our experimental flows, dependent on a bulk inertial number. On the second, acoustic fluidisation is one of many possible explanations suggested for the low effective friction necessary to explain many geophysical flows' long runouts (Davies, 1982; Lucas et al., 2014), but we are not aware of it having been previously demonstrated without the application of external forcing. As Figure 7a illustrates, our measurements of μ show the effective friction taking values on the plate lower than the channel incline $\tan \theta$, which is implied to be its approximate off-plate value by both the downslope uniformity of the flow at the sidewalls and the saturation of flow velocity observed at the surface. Since the base's roughness is identical in each location, we believe it possible that this reduced friction is associated with the strong acoustic vibrations of the plate, induced by the flow itself.

Acknowledgments

This work was primarily funded by project ERC-CG-2013-PE10-617472 SLIDEQUAKES, with supporting funds from La Société des Amis de l'ESPCI and from IPGP. The authors are aware of no conflict of interest. Experimental data are available at the Pangaea repository (Arran et al., 2020), while computations were performed and plots produced with the summary data and code at Zenodo (Arran et al., 2021), using NumPy (Harris et al., 2020), Matplotlib (Hunter, 2007), and pandas (McKinney, 2010). We are grateful to Abdelhak Souilah for his construction of the experimen-

tal apparatus and to Kate Allstadt, Florent Gimbert, and two anonymous reviewers for their detailed and constructive comments on the manuscript.

References

- Akaike, H. (1971). *Determination of the number of factors by an extended maximum likelihood principle* (Tech. Rep.). Inst. Statist. Math.
- Akaike, H. (1974). A new look at the statistical model identification. *IEEE Transactions on Automatic Control*, 19(6), 716–723. Retrieved from <https://link.springer.com/content/pdf/10.1007%2F978-1-4612-1694-0.pdf>
- Akaike, H. (1978). On the likelihood of a time series model. *Journal of the Royal Statistical Society. Series D (The Statistician)*, 27(3/4), 217–235. Retrieved from <http://www.jstor.org/stable/2988185>
- Allstadt, K. E., Farin, M., Iverson, R. M., Obryk, M. K., Kean, J. W., Tsai, V. C., ... Logan, M. (2020). Measuring basal force fluctuations of debris flows using seismic recordings and empirical green's functions. *Journal of Geophysical Research: Earth Surface*, 125(9), e2020JF005590. Retrieved from <https://agupubs.onlinelibrary.wiley.com/doi/abs/10.1029/2020JF005590> (e2020JF005590 2020JF005590) doi: 10.1029/2020JF005590
- Allstadt, K. E., Matoza, R. S., Lockhart, A. B., Moran, S. C., Caplan-Auerbach, J., Haney, M. M., ... Malone, S. D. (2018). Seismic and acoustic signatures of surficial mass movements at volcanoes. *Journal of Volcanology and Geothermal Research*, 364, 76–106. Retrieved from <http://www.sciencedirect.com/science/article/pii/S0377027317306261> doi: 10.1016/j.jvolgeores.2018.09.007
- Arran, M. I., Mangeney, A., de Rosny, J., Farin, M., Toussaint, R., & Roche, O. (2020). *IPGP laboratory data on granular flows' high-frequency seismic signals* [data set]. PANGAEA. Retrieved from <https://doi.org/10.1594/PANGAEA.924870> doi: 10.1594/PANGAEA.924870
- Arran, M. I., Mangeney, A., de Rosny, J., Farin, M., Toussaint, R., & Roche, O. (2021). *Laboratory landquakes, v1.0*. Zenodo. doi: 10.5281/zenodo.4044233
- Babic, M. (1997). Average balance equations for granular materials. *International Journal of Engineering Science*, 35(5), 523–548. Retrieved from <http://www.sciencedirect.com/science/article/pii/S0020722596000948> doi: 10.1016/S0020-7225(96)00094-8
- Bachelet, V. (2018). *Étude expérimentale des émissions acoustiques générées par les écoulements granulaires* (Doctoral dissertation, Institut de Physique du Globe de Paris). Retrieved from <https://hal.archives-ouvertes.fr/tel-03104582>
- Bachelet, V., Mangeney, A., Toussaint, R., DeRosny, J., Farin, M., & Hibert, C. (2021). Acoustic emissions of nearly steady and uniform granular flows: a proxy for flow dynamics and velocity fluctuations. *Journal of Geophysical Research: Earth Surface*, (Under review). Retrieved from <https://arxiv.org/pdf/2101.04161.pdf>
- Börzsönyi, T., & Ecke, R. E. (2006, December). Rapid granular flows on a rough incline: phase diagram, gas transition, and effects of air drag. *Physical Review E*, 74(6 Pt 1), 061301. Retrieved from <https://doi.org/10.1103/PhysRevE.74.061301> doi: 10.1103/physreve.74.061301
- Capozza, R., Vannossi, A., Vezzani, A., & Zapperi, S. (2009). Suppression of friction by mechanical vibrations. *Physical Review Letters*, 103, 085502. doi: 10.1103/PhysRevLett.103.085502
- Ciarlet, P. G. (1997). Chapter 1 - linearly elastic plates. In P. G. Ciarlet (Ed.), *Mathematical elasticity* (Vol. 27, p. 3–127). Elsevier. Retrieved from <http://www.sciencedirect.com/science/article/pii/S0168202497800070> doi: 10.1016/S0168-2024(97)80007-0

- Clark, A. H., & Dijkstra, J. A. (2020). Editorial: Non-local modeling and diverging lengthscales in structured fluids. *Frontiers in Physics*, 8, 18. Retrieved from <https://www.frontiersin.org/article/10.3389/fphy.2020.00018> doi: 10.3389/fphy.2020.00018
- Cuomo, S. (2020). Modelling of flowslides and debris avalanches in natural and engineered slopes: a review. *Geoenvironmental Disasters*, 7(1).
- da Cruz, F., Emam, S., Prochnow, M., Roux, J.-N., & Chevoir, F. (2005). Rheophysics of dense granular materials: Discrete simulation of plane shear flows. *Physical Review E*, 72, 021309. Retrieved from <https://link.aps.org/doi/10.1103/PhysRevE.72.021309> doi: 10.1103/PhysRevE.72.021309
- Dahlen, F. A. (1993). Single-force representation of shallow landslide sources. *Bulletin of the Seismological Society of America*, 83(1), 130. Retrieved from <http://dx.doi.org/>
- Dammeier, F., Moore, J. R., Hammer, C., Haslinger, F., & Loew, S. (2016). Automatic detection of alpine rockslides in continuous seismic data using hidden markov models. *Journal of Geophysical Research: Earth Surface*, 121(2), 351–371. Retrieved from <https://agupubs.onlinelibrary.wiley.com/doi/abs/10.1002/2015JF003647> doi: 10.1002/2015JF003647
- Dammeier, F., Moore, J. R., Haslinger, F., & Loew, S. (2011). Characterization of alpine rockslides using statistical analysis of seismic signals. *Journal of Geophysical Research: Earth Surface*, 116(F4). Retrieved from <https://agupubs.onlinelibrary.wiley.com/doi/abs/10.1029/2011JF002037> doi: 10.1029/2011JF002037
- Davies, T. R. H. (1982). Spreading of rock avalanche debris by mechanical fluidization. *Rock mechanics*, 15, 9–24.
- Delannay, R., Valance, A., Mangeney, A., Roche, O., & Richard, P. (2017). Granular and particle-laden flows: from laboratory experiments to field observations. *Journal of Physics D: Applied Physics*, 50(5), 053001. Retrieved from <https://doi.org/10.1088%2F1361-6463%2F50%2F5%2F053001> doi: 10.1088/1361-6463/50/5/053001
- Deparis, J., Jongmans, D., Cotton, F., Baillet, L., Thouvenot, F., & Hantz, D. (2008, 08). Analysis of Rock-Fall and Rock-Fall Avalanche Seismograms in the French Alps. *Bulletin of the Seismological Society of America*, 98(4), 1781–1796. Retrieved from <https://doi.org/10.1785/0120070082> doi: 10.1785/0120070082
- Dijkstra, J. A., Wortel, G. H., van Dellen, L. T. H., Dauchot, O., & van Hecke, M. (2011). Jamming, yielding, and rheology of weakly vibrated granular media. *Physical Review Letters*, 107, 108303. Retrieved from <https://link.aps.org/doi/10.1103/PhysRevLett.107.108303> doi: 10.1103/PhysRevLett.107.108303
- Farin, M., Mangeney, A., de Rosny, J., Toussaint, R., & Trinh, P.-T. (2018). Link between the dynamics of granular flows and the generated seismic signal: Insights from laboratory experiments. *Journal of Geophysical Research: Earth Surface*, 123(6), 1407–1429. Retrieved from <https://agupubs.onlinelibrary.wiley.com/doi/abs/10.1029/2017JF004296> doi: 10.1029/2017JF004296
- Farin, M., Mangeney, A., de Rosny, J., Toussaint, R., & Trinh, P.-T. (2019). Relations between the characteristics of granular column collapses and resultant high-frequency seismic signals. *Journal of Geophysical Research: Earth Surface*, 124(12), 2987–3021. Retrieved from <https://agupubs.onlinelibrary.wiley.com/doi/abs/10.1029/2019JF005258> doi: 10.1029/2019JF005258
- Farin, M., Tsai, V. C., Lamb, M. P., & Allstadt, K. E. (2019). A physical model of the high-frequency seismic signal generated by debris flows. *Earth Surface Processes and Landforms*, 44(13), 2529–2543. Retrieved from <https://onlinelibrary.wiley.com/doi/abs/10.1002/esp.4677> doi: 10.1002/esp.4677

- 10.1002/esp.4677
- Ferdowsi, B., Griffa, M., Guyer, R., Johnson, P., & Carmeliet, J. (2014). Effect of boundary vibration on the frictional behavior of a dense sheared granular layer. *Acta Mechanica*, 225, 2227–2237.
- Fernández-Nieto, E., Garres-Díaz, J., Mangeney, A., & Narbona-Reina, G. (2018). 2d granular flows with the $\mu(i)$ rheology and side walls friction: A well-balanced multilayer discretization. *Journal of Computational Physics*, 356, 192–219. Retrieved from <https://www.sciencedirect.com/science/article/pii/S0021999117308823> doi: 10.1016/j.jcp.2017.11.038
- Fleming, R., Taylor, F., & (U.S.), G. S. (1980). *Estimating the costs of landslide damage in the united states*. U.S. Department of the Interior, Geological Survey. Retrieved from <https://books.google.fr/books?id=DGnlhWP6h8cC>
- Froude, M. J., & Petley, D. N. (2018). Global fatal landslide occurrence from 2004 to 2016. *Nat. Hazards Earth Syst. Sci.*, 18, 2161–2181.
- Fuchs, F., Lenhardt, W., Bokelmann, G., & the AlpArray Working Group. (2018). Seismic detection of rockslides at regional scale: examples from the eastern alps and feasibility of kurtosis-based event location. *Earth Surface Dynamics*, 6. doi: 10.5194/esurf-6-955-2018
- Fukao, Y. (1995, 07). Single-force representation of earthquakes due to landslides or the collapse of caverns. *Geophysical Journal International*, 122(1), 243–248. Retrieved from <https://doi.org/10.1111/j.1365-246X.1995.tb03551.x> doi: 10.1111/j.1365-246X.1995.tb03551.x
- Gardel, E., Sitaridou, E., Facto, K., Keene, E., Hattam, K., Easwar, N., & Menon, N. (2009). Dynamical fluctuations in dense granular flows. *Philosophical Transactions of the Royal Society A: Mathematical, Physical and Engineering Sciences*, 367(1909), 5109–5121. Retrieved from <https://royalsocietypublishing.org/doi/abs/10.1098/rsta.2009.0189> doi: 10.1098/rsta.2009.0189
- Garve, T. W. (1925). Segregation in bins. *J. Amer. Ceram. Soc.*, 80, 666.
- GDR MiDi. (2004, August 01). On dense granular flows. *The European Physical Journal E*, 14(4), 341–365. Retrieved from <https://doi.org/10.1140/epje/i2003-10153-0> doi: 10.1140/epje/i2003-10153-0
- Gimbert, F., Fuller, B. M., Lamb, M. P., Tsai, V. C., & Johnson, J. P. L. (2019). Particle transport mechanics and induced seismic noise in steep flume experiments with accelerometer-embedded tracers. *Earth Surface Processes and Landforms*, 44(1), 219–241. Retrieved from <https://onlinelibrary.wiley.com/doi/abs/10.1002/esp.4495> doi: 10.1002/esp.4495
- Gimbert, F., & Tsai, V. C. (2015). Predicting short-period, wind-wave-generated seismic noise in coastal regions. *Earth and Planetary Science Letters*, 426, 280–292. Retrieved from <http://www.sciencedirect.com/science/article/pii/S0012821X15003738> doi: 10.1016/j.epsl.2015.06.017
- Given, D. D., Allen, R. M., Baltay, A. S., Bodin, P., Cochran, E. S., Creager, K., ... Yelin, T. S. (2018). *Revised technical implementation plan for the shakealert system—an earthquake early warning system for the west coast of the united states* (Tech. Rep.). U.S. Geological Survey Open-File Report. doi: 10.3133/ofr20181155
- Goldhirsch, I. (2003). Rapid granular flows. *Annual Review of Fluid Mechanics*, 35(1), 267–293. Retrieved from <https://doi.org/10.1146/annurev.fluid.35.101101.161114> doi: 10.1146/annurev.fluid.35.101101.161114
- Gollin, D., Berzi, D., & Bowman, E. (2017). Extended kinetic theory applied to inclined granular flows: role of boundaries. *Granular Matter*, 19(56).
- Gray, J. M. N. T. (2018). Particle Segregation in Dense Granular Flows. *Annual Review of Fluid Mechanics*, 50(1), 407–433. Retrieved from <https://doi.org/10.1146/annurev-fluid-122316-045201> doi: 10.1146/annurev-fluid-122316-045201

- Guzzetti, F., Gariano, S. L., Peruccacci, S., Brunetti, M. T., Marchesini, I., Rossi, M., & Melillo, M. (2020). Geographical landslide early warning systems. *Earth-Science Reviews*, 200, 102973. Retrieved from <http://www.sciencedirect.com/science/article/pii/S0012825219304635> doi: 10.1016/j.earscirev.2019.102973
- Hanes, D. M., & Walton, O. R. (2000). Simulations and physical measurements of glass spheres flowing down a bumpy incline. *Powder Technology*, 109(1), 133–144. Retrieved from <http://www.sciencedirect.com/science/article/pii/S0032591099002326> doi: 10.1016/S0032-5910(99)00232-6
- Harris, C. R., Millman, K. J., van der Walt, S. J., Gommers, R., Virtanen, P., Cournapeau, D., ... Oliphant, T. E. (2020, September). Array programming with NumPy. *Nature*, 585(7825), 357–362. Retrieved from <https://doi.org/10.1038/s41586-020-2649-2> doi: 10.1038/s41586-020-2649-2
- Hertz, H. R. (1881). Über die berührung fester elastischer körper. *Journal für die reine und angewandte Mathematik*, 92, 156–171. Retrieved from <https://home.uni-leipzig.de/pwm/web/download/Hertz1881.pdf>
- Hervás, J. E. (2003). *Lessons learnt from landslide disasters in europe. eur 20558 en* (Tech. Rep.). Ispra, Italy: European Commission.
- Hibert, C., Ekström, G., & Stark, C. P. (2017). The relationship between bulk-mass momentum and short-period seismic radiation in catastrophic landslides. *Journal of Geophysical Research: Earth Surface*, 122(5), 1201–1215. Retrieved from <https://agupubs.onlinelibrary.wiley.com/doi/abs/10.1002/2016JF004027> doi: 10.1002/2016JF004027
- Hibert, C., Mangeney, A., Grandjean, G., Baillard, C., Rivet, D., Shapiro, N. M., ... Crawford, W. (2014). Automated identification, location, and volume estimation of rockfalls at piton de la fournaise volcano. *Journal of Geophysical Research: Earth Surface*, 119(5), 1082–1105. Retrieved from <https://agupubs.onlinelibrary.wiley.com/doi/abs/10.1002/2013JF002970> doi: 10.1002/2013JF002970
- Hibert, C., Mangeney, A., Grandjean, G., & Shapiro, N. M. (2011). Slope instabilities in Dolomieu crater, Réunion Island: From seismic signals to rockfall characteristics. *Journal of Geophysical Research: Earth Surface*, 116(F4). doi: 10.1029/2011JF002038
- Hibert, C., Stark, C. P., & Ekström, G. (2015). Dynamics of the oso-steelehead landslide from broadband seismic analysis. *Natural Hazards and Earth System Sciences*, 15(6), 1265–1273. Retrieved from <https://www.nat-hazards-earth-syst-sci.net/15/1265/2015/> doi: 10.5194/nhess-15-1265-2015
- Hsu, L., Dietrich, W. E., & Sklar, L. S. (2014). Mean and fluctuating basal forces generated by granular flows: Laboratory observations in a large vertically rotating drum. *Journal of Geophysical Research: Earth Surface*, 119(6), 1283–1309. Retrieved from <https://agupubs.onlinelibrary.wiley.com/doi/abs/10.1002/2013JF003078> doi: 10.1002/2013JF003078
- Hungr, O., & Morgenstern, N. R. (1984). Experiments on the flow behaviour of granular materials at high velocity in an open channel. *Géotechnique*, 34(3), 405–413. Retrieved from <https://doi.org/10.1680/geot.1984.34.3.405> doi: 10.1680/geot.1984.34.3.405
- Hunter, J. D. (2007). Matplotlib: A 2d graphics environment. *Computing in Science & Engineering*, 9(3), 90–95. doi: 10.1109/MCSE.2007.55
- Hurvich, C. M., & Tsai, C.-L. (1989). Regression and time series model selection in small samples. *Biometrika*, 76(2), 297–307. Retrieved from <https://doi.org/10.1093/biomet/76.2.297> doi: 10.1093/biomet/76.2.297
- Jing, L., Kwok, C. Y., Leung, Y. F., & Sobral, Y. D. (2016). Characterization of base roughness for granular chute flows. *Physical Review E*, 94, 052901. Retrieved from <https://link.aps.org/doi/10.1103/PhysRevE.94.052901> doi: 10.1103/PhysRevE.94.052901

- John Steel. (2019). *Fiche technique acier s355* (Tech. Rep.). Author. Retrieved from <https://www.john-steel.com/fr/acier/29-plaque-d-acier-decape-et-graisse.html>
- Johnson, P. A., Savage, H., Knuth, M., Gomberg, J., & Marone, C. (2008). Effects of acoustic waves on stick-slip in granular media and implications for earthquakes. *Nature*, *451*, 57–60.
- Jop, P., Forterre, Y., & Pouliquen, O. (2005). Crucial role of sidewalls in granular surface flows: consequences for the rheology. *Journal of Fluid Mechanics*, *541*, 167–192. doi: 10.1017/S0022112005005987
- Jop, P., Forterre, Y., & Pouliquen, O. (2006, June). A constitutive law for dense granular flows. *Nature*, *441*(7094), 727–730. Retrieved from <http://www.nature.com/nature/journal/v441/n7094/suppinfo/nature04801\..S1.html> (10.1038/nature04801) doi: 10.1038/nature04801
- Kanamori, H., & Given, J. W. (1982). Analysis of long-period seismic waves excited by the may 18, 1980, eruption of mount st. helens—a terrestrial monopole? *Journal of Geophysical Research: Solid Earth*, *87*(B7), 5422–5432. Retrieved from <https://agupubs.onlinelibrary.wiley.com/doi/abs/10.1029/JB087iB07p05422> doi: 10.1029/JB087iB07p05422
- Kawakatsu, H. (1989). Centroid single force inversion of seismic waves generated by landslides. *Journal of Geophysical Research: Solid Earth*, *94*(B9), 12363–12374. Retrieved from <https://agupubs.onlinelibrary.wiley.com/doi/abs/10.1029/JB094iB09p12363> doi: 10.1029/JB094iB09p12363
- Kean, J. W., Coe, J. A., Coviello, V., Smith, J. B., McCoy, S. W., & Arattano, M. (2015). Estimating rates of debris flow entrainment from ground vibrations. *Geophysical Research Letters*, *42*(15), 6365–6372. Retrieved from <https://agupubs.onlinelibrary.wiley.com/doi/abs/10.1002/2015GL064811> doi: 10.1002/2015GL064811
- Kim, D. H., Gratchev, I., Berends, J., & Balasubramaniam, A. (2015). Calibration of restitution coefficients using rockfall simulations based on 3d photogrammetry model: a case study. *Natural Hazards*, *78*, 1931–1946. Retrieved from <https://doi.org/10.1007/s11069-015-1811-x>
- Kullback, S., & Leibler, R. A. (1951). On information and sufficiency. *Ann. Math. Statist.*, *22*(1), 79–86. Retrieved from <https://doi.org/10.1214/aoms/1177729694> doi: 10.1214/aoms/1177729694
- Lai, V. H., Tsai, V. C., Lamb, M. P., Ulizio, T. P., & Beer, A. R. (2018, 06). The seismic signature of debris flows: Flow mechanics and early warning at montecito, california. *Geophysical Research Letters*, *45*(11), p5528–5535. doi: 10.1029/2018GL077683
- Lamb, H. (1904). On the Propagation of Tremors over the Surface of an Elastic Solid. *Philosophical Transactions of the Royal Society of London A: Mathematical, Physical and Engineering Sciences*, *203*(359-371), 1–42. Retrieved from <http://rsta.royalsocietypublishing.org/content/203/359-371/1> doi: 10.1098/rsta.1904.0013
- Lastakowski, H., Géminard, J.-C., & Vidal, V. (2015). Granular friction: Triggering large events with small vibrations. *Scientific Reports*, *5*, 13455.
- Lee, E.-J., Liao, W.-Y., Lin, G.-W., Chen, P., Mu, D., & Lin, C.-W. (2019). Towards automated real-time detection and location of large-scale landslides through seismic waveform back projection. *Geofluids*. doi: 10.1155/2019/1426019
- Lemrich, L., Carmeliet, J., Johnson, P. A., Guyer, R., & Jia, X. (2017). Dynamic induced softening in frictional granular materials investigated by discrete-element-method simulation. *Physical Review E*, *96*, 062901. Retrieved from <https://link.aps.org/doi/10.1103/PhysRevE.96.062901> doi: 10.1103/PhysRevE.96.062901
- Levy, C., Mangeney, A., Bonilla, F., Hibert, C., Calder, E. S., & Smith, P. J. (2015).

- Friction weakening in granular flows deduced from seismic records at the soufrière hills volcano, montserrat. *Journal of Geophysical Research: Solid Earth*, 120(11), 7536–7557. Retrieved from <https://agupubs.onlinelibrary.wiley.com/doi/abs/10.1002/2015JB012151> doi: 10.1002/2015JB012151
- Love, A. E. H., & Darwin, G. H. (1888). Xvi. the small free vibrations and deformation of a thin elastic shell. *Philosophical Transactions of the Royal Society of London. (A.)*, 179, 491–546. Retrieved from <https://royalsocietypublishing.org/doi/abs/10.1098/rsta.1888.0016> doi: 10.1098/rsta.1888.0016
- Lucas, A., Mangeney, A., & Ampuero, J. P. (2014). Frictional velocity-weakening in landslides on earth and on other planetary bodies. *Nature Communications*, 5, 3417. doi: 10.1038/ncomms4417
- Léopoldès, J., Jia, X., Tourin, A., & Mangeney, A. (2020, Oct). Triggering granular avalanches with ultrasound. *Phys. Rev. E*, 102, 042901. Retrieved from <https://link.aps.org/doi/10.1103/PhysRevE.102.042901> doi: 10.1103/PhysRevE.102.042901
- McCoy, S. W., Tucker, G. E., Kean, J. W., & Coe, J. A. (2013). Field measurement of basal forces generated by erosive debris flows. *Journal of Geophysical Research: Earth Surface*, 118(2), 589–602. Retrieved from <https://agupubs.onlinelibrary.wiley.com/doi/abs/10.1002/jgrf.20041> doi: 10.1002/jgrf.20041
- McKinney, W. (2010). Data Structures for Statistical Computing in Python. In S. van der Walt & J. Millman (Eds.), *Proceedings of the 9th Python in Science Conference* (p. 56–61). doi: 10.25080/Majora-92bf1922-00a
- McLaskey, G. C., & Glaser, S. D. (2010). Hertzian impact: Experimental study of the force pulse and resulting stress waves. *The Journal of the Acoustical Society of America*, 128(3), 1087–1096. Retrieved from <https://asa.scitation.org/doi/abs/10.1121/1.3466847> doi: 10.1121/1.3466847
- Michlmayr, G., & Or, D. (2014, October 01). Mechanisms for acoustic emissions generation during granular shearing. *Granular Matter*, 16(5), 627–640. Retrieved from <https://doi.org/10.1007/s10035-014-0516-2> doi: 10.1007/s10035-014-0516-2
- Miller, G. F., & Pursey, H. (1954). The Field and Radiation Impedance of Mechanical Radiators on the Free Surface of a Semi-Infinite Isotropic Solid. *Proceedings of the Royal Society of London A: Mathematical, Physical and Engineering Sciences*, 223(1155), 521–541. Retrieved from <http://rspa.royalsocietypublishing.org/content/223/1155/521> doi: 10.1098/rspa.1954.0134
- National Research Council. (1985). *Reducing losses from landsliding in the united states*. The National Academies Press.
- Nishiguchi, Y., Uchida, T., Takezawa, N., Ishizuka, T., & Mizuyama, T. (2012). Runout characteristics and grain size distribution of large-scale debris flows triggered by deep catastrophic landslides. *International Journal of Erosion Control Engineering*, 5(1), 16–26. doi: 10.13101/ijece.5.16
- Norris, R. D. (1994). Seismicity of rockfalls and avalanches at three cascade range volcanoes: Implications for seismic detection of hazardous mass movements. *Bulletin of the Seismological Society of America*, 84(6), 1925. Retrieved from <http://dx.doi.org/>
- Plancherel, M., & Mittag-Leffler, G. (1910). Contribution à l'étude de la représentation d'une fonction arbitraire par les intégrales définies. *Rendiconti del Circolo Matematico di Palermo*, 30(1), 289–335.
- Pudasaini, S., & Hutter, K. (2006). *Avalanche dynamics: Dynamics of rapid flows of dense granular avalanches*. Springer. Retrieved from <https://books.google.co.uk/books?id=gri6NAEACAAJ>
- Roche, O., van den Wildenberg, S., Valance, A., Delannay, R., Mangeney, A., Corna,

- L., & Latchimy, T. (2021). Experimental assessment of the effective friction at the base of granular chute flows on smooth incline. *Physical Review E, (Under review)*. Retrieved from <https://arxiv.org/abs/2103.01154>
- Schneider, D., Bartelt, P., Caplan-Auerbach, J., Christen, M., Huggel, C., & McArdell, B. W. (2010). Insights into rock-ice avalanche dynamics by combined analysis of seismic recordings and a numerical avalanche model. *Journal of Geophysical Research: Earth Surface*, 115(F4). Retrieved from <https://agupubs.onlinelibrary.wiley.com/doi/abs/10.1029/2010JF001734> doi: 10.1029/2010JF001734
- Scholl, H. J., Ballard, S., Carnes, S., Herman, A., & Parker, N. (2017). Informational challenges in early disaster response: The massive oso/sr530 landslide 2014 as case in point. *Proceedings of the 50th Hawaii International Conference on System Sciences*.
- Schuster, R. L., & Fleming, R. W. (1986). Economic losses and fatalities due to landslides. *Bulletin of the Association of Engineering Geologists*, 23(1), p11–28.
- Sigmund Lindner. (2018). *Product data sheet*. Retrieved online. Retrieved from <https://www.sigmund-lindner.com/en/products/glass-beads/dispersing-beads/>
- Silbert, L. E., Ertas, D., Grest, G. S., Halsey, T. C., Levine, D., & Plimpton, S. J. (2001). Granular flow down an inclined plane: Bagnold scaling and rheology. *Physical Review E*, 64, 051302. Retrieved from <https://link.aps.org/doi/10.1103/PhysRevE.64.051302> doi: 10.1103/PhysRevE.64.051302
- Steel SS. (2019). *Data table for carbon steel s355mc* (Tech. Rep.). Author. Retrieved from <https://www.steelss.com/Carbon-steel/s355mc.html>
- Suriñach, E., Vilajosana, I., Khazaradze, G., Biescas, B., Furdada, G., & Vilaplana, J. M. (2005). Seismic detection and characterization of landslides and other mass movements. *Natural Hazards and Earth System Sciences*, 5(6), 791–798. Retrieved from <https://www.nat-hazards-earth-syst-sci.net/5/791/2005/> doi: 10.5194/nhess-5-791-2005
- Taberlet, N., Richard, P., Jenkins, J. T., & Delannay, R. (2007). Density inversion in rapid granular flows: the supported regime. *Eur. Phys. J. E*, 22(1), 17–24. Retrieved from <https://doi.org/10.1140/epje/e2007-00010-5> doi: 10.1140/epje/e2007-00010-5
- Takahashi, T. (1981). Debris flow. *Annual Review of Fluid Mechanics*, 13(1), 57–77. Retrieved from <https://doi.org/10.1146/annurev.fl.13.010181.000421> doi: 10.1146/annurev.fl.13.010181.000421
- Taylor, S., & Brodsky, E. E. (2017). Granular temperature measured experimentally in a shear flow by acoustic energy. *Physical Review E*, 96, 032913. Retrieved from <https://link.aps.org/doi/10.1103/PhysRevE.96.032913> doi: 10.1103/PhysRevE.96.032913
- Tsai, V. C., & Atiganyanun, S. (2014, 09). Green’s Functions for Surface Waves in a Generic Velocity Structure. *Bulletin of the Seismological Society of America*, 104(5), 2573–2578. Retrieved from <https://doi.org/10.1785/0120140121> doi: 10.1785/0120140121
- Tsai, V. C., Minchew, B., Lamb, M. P., & Ampuero, J.-P. (2012). A physical model for seismic noise generation from sediment transport in rivers. *Geophysical Research Letters*, 39(2). Retrieved from <https://agupubs.onlinelibrary.wiley.com/doi/abs/10.1029/2011GL050255> doi: 10.1029/2011GL050255
- Tsang, J. M. F., Dalziel, S. B., & Vriend, N. M. (2019). The granular Blasius problem. *Journal of Fluid Mechanics*, 872, 784–817. doi: 10.1017/jfm.2019.357
- van Asch, T., Malet, J., van Beek, L., & Amitrano, D. (2007). Techniques, advances, problems and issues in numerical modelling of landslide hazard. *Bulletin de la Société Géologique de France*, 178(2), p65–88.

Supporting Information for “Laboratory Landquakes: Insights from experiments into the high-frequency seismic signal generated by geophysical granular flows”

M. I. Arran^{1,*}, A. Mangeney¹, J. De Rosny², M. Farin², R. Toussaint^{3,4}, O. Roche⁵

¹Université de Paris, Institut de physique du globe de Paris, CNRS, F-75005 Paris, France

²Institut Langevin, ESPCI Paris, PSL University, CNRS, 75005 Paris, France

³Université de Strasbourg, CNRS, Institut Terre et Environnement de Strasbourg, UMR 7063, F-67084 Strasbourg, France

⁴SFF PoreLab, The Njord Centre, Department of Physics, University of Oslo, Oslo, Norway

⁵Université Clermont Auvergne, CNRS, IRD, OPGC, Laboratoire Magmas et Volcans, F-63000 Clermont-Ferrand, France.

*Corresponding author: Matthew Arran, arran@ipgp.fr

Contents of this file

1. Text S1 to S10
2. Figures S1 to S6
3. Table S1

Additional Supporting Information (Files uploaded separately)

1. Captions for Movies S1 to S2

Introduction

To supplement the text of “Laboratory Landquakes”, we gather here a collection of appendices to the text; figures and a table associated with these appendices; and descriptions of two videos that provide supplementary illustration. In section S1, we list and define the notation used in the article’s text. Section S2 describes and justifies conditions for the validity of the ‘stochastic impact’ framework that’s described in section 1.2, for predicting a granular flow’s seismic signal, while section S3 reviews the use of Hertz theory to describe binary, elastic, quasistatic, normal interactions between spheres. We describe in sections S4 and S5, respectively, the amplifier settings used in experiments and the experimental control system, while sections S6 and S7 describe the derivation, calibration, and validation of relations linking experimental measurements to i) the net force applied by each flow to the instrumented plate and ii) the power spectrum of this force’s normal component. Section S8 describes the processing of high-speed camera images to extract base-normal profiles of flow properties at the channel wall, S9 describes the statistical tools used to analyse our experimental results, and section S10 demonstrates the importance of the Green’s function in the interpretation of landquake signals.

Figure S1 is associated with section S3, Figure S2 with section S5, Figure S3 with section S6, and Figures S4 and S5 with section S7. Table S1 is associated with section S9 and Figure S6 with section S10. Finally, the mp4 videos available as supplementary material illustrate section S8 and are described at Movie S1 and Movie S2.

S1. Notation

f, t, \mathbf{x} : Frequency, time, source position
 P : The power spectral density of a quantity \cdot
 $\tilde{\cdot}$: The Fourier transform of \cdot over time interval Δt
 $\langle \cdot \rangle_{\Delta t}$: The arithmetic mean of \cdot over the interval Δt
 $\langle \cdot \rangle_{\Delta f}$: The moving average of $\tilde{\cdot}$ over a frequency window Δf
 v_r : The landquake velocity signal at a receiver at \mathbf{r} , radius r from the source
 n_I : The number of impacts per unit volume and per unit time
 \mathbf{F}_I : The force exerted by a representative impact
 \mathbf{G} : The Green’s function linking \mathbf{F}_I to v_r
 A, ϕ : The area and particle volume fraction of a granular flow
 ρ, d, u : The density, diameter, and downslope speed of a representative particle
 $\Delta p, \mathbf{e}_I$: The magnitude and direction of the impulse of a representative impact
 h, \bar{u} : The depth and depth-averaged mean velocity of a flow
 E, ν : The Young’s modulus and Poisson’s ratio of a particle’s material
 $\tau(u_n)$: The timescale of a Hertzian impact at normal velocity u_n
 ζ : The normalised, non-dimensional spectral density of the normal force between particles undergoing a Hertzian impact
 u_j, T_j, z_j : The mean velocity, granular temperature, and base-normal position of particles in a flow’s j th layer
 h_g : The experimental flow’s depth at its point of outflow from the reservoir
 W, θ : The width and inclination angle of the experimental channel
 X, Y, H : The length, width, and thickness of the instrumented plate

F_x, F_z : The downslope and base-normal forces exerted by the flow on the plate
 g : The magnitude of gravitational acceleration
 $t_d, \Delta t_c$: The time delay before, and the duration of, the high-speed camera’s recording
 σ : The average mass per unit area overlying the instrumented plate, over time Δt_c
 μ : The effective friction between the instrumented plate and the overlying flow
 M : The cumulative mass outflow through the channel, as measured by the mass balance
 q : The average mass flux through the channel, per unit width, over time Δt_c
 ρ_p, E_p, ν_p : The density, Young’s modulus, and Poisson’s ratio of the instrumented plate
 D, Δ_f : The plate’s bending stiffness and the mean frequency gap between its resonances
 \mathcal{P} : The proportion of the plate’s energy in its measurable vertical motion
 Q : The quality factor for the attenuation of the plate’s energy
 a_j : The acceleration measured by the instrumented plate’s j th accelerometer
 x_j, z_j, \mathbf{u}_j : The downslope position, base-normal height, and velocity of a particle tracked at the channel’s sidewall
 $C(\cdot; z)$: A normalised coarse-graining function, localised around z
 $\phi_w(z), \mathbf{u}_w(z), T_w(z)$: Depth-profiles of the mean relative volume fraction, velocity, and granular temperature of particles tracked at the channel’s sidewall
 u_w, \bar{u}_w : The downslope component of \mathbf{u}_w and its depth-averaged value
 P_F : The power spectral density of the normal force exerted by a flow on its base
 P_F^0 : The amplitude of P_F at signal periods much larger than the timescale of individual impacts but less than that of the flow’s evolution
 f_c : The corner frequency of P_F , at which it falls below half its maximum value
 $\hat{\cdot}$: A model’s prediction for the quantity \cdot
 K : An unspecified prefactor in the model of Kean et al. (2015)
 e : The coefficient of restitution of particles’ impacts in the model of Farin, Tsai, Lamb, and Allstadt (2019)
 v : The normalised standard deviation of base-impacting particles’ velocities
 $\xi(v)$: A non-dimensional prefactor accounting for variation in impacts’ geometry in the models of Farin et al. (2019)
 χ : A shape factor for basal particle’s mean downslope velocity, in the ‘thick-flow’ model
 γ : A constant of attenuation, with an impact’s base-normal height, for the squared impulse it transfers to the base, in the model of Bachelet et al.
 ϵ : The typical factor of error in a model’s predictions of P_F^0
 I, \hat{I} : The inertial number within a flow and a bulk estimate for its value
 δF : The high-frequency fluctuating force exerted by the flow on the instrumented plate
 $\delta \mathcal{F}^2$: The ratio between i) the mean of δF^2 and ii) the squared mean force
 Π_s : The total high-frequency seismic power transferred by the flow to the plate
 ρ_g, c_s : The density and shear wave velocity of an idealised Earth
 $t_r - t_s$: The source-receiver delay of an idealised Green’s function

S2. The Stochastic Impact Framework

Here, we discuss the ‘stochastic impact’ framework: consideration of the total seismic signal as a sum of the uncorrelated signals generated by individual particle impacts, with the properties of the impacts determined by mean properties of the flow and with a specified Green’s function mapping the force of an individual impact to the seismic signal observed at a remote station. By doing so, we hope to indicate its range of validity, by making clear the assumptions on which it rests: that the signal originates mainly from particle impacts; that materials are sufficiently stiff for the total signal to be the sum of signals from individual impacts; that the area considered is sufficiently extensive or the frequencies considered sufficiently high for impacts’ signals to be uncorrelated; and that the spatial and temporal intervals between impacts are much smaller than the length and time scales of variation both of the flow and of the Green’s function for signal propagation, so that a single impact force and Green’s function may be used to represent all impacts.

S2.1. Impacts Must be the Dominant Source of the Signal

Most obviously, for a model of individual impacts to describe the seismic signal generated by a geophysical granular flow, other sources (e.g. those described by Michlmayr and Or (2014)) must be less significant. For example, we would not expect the model to apply to rockslides, for which basal friction is expected to be the dominant source, or to soil creep, for which the rupture of soil fibres would be more significant.

S2.2. The Signal Must be a Sum of Individual Impact Signals

Next, we must be able to consider impacts separately, with negligible interactions between them and hence a total signal equal to the sum of the individual signals. This will be the case if the deformation due to one impact at the site of a second is small compared to the local deformation due to that second impact. Or, writing $\epsilon(\mathbf{x}, \mathbf{x}_1)$ for deformation at x due to the impact at \mathbf{x}_1 , we require $\epsilon(\mathbf{x}_2, \mathbf{x}_1) \ll \epsilon(\mathbf{x}_2, \mathbf{x}_2)$. Since $\|\mathbf{x}_2 - \mathbf{x}_1\|$ is at least a particle radius, this will be the case if deformation is limited to within a particle radius, so if the impacted material is sufficiently stiff. It will not be the case for, for example, rockfalls onto sandbeds, for which the crater caused by one rock’s impact will affect the impact of another.

S2.3. Impact Signals Must be Uncorrelated

For the framework to work, we next require that the signals from different impacts must be uncorrelated in Fourier space. If, in frequency space, $\tilde{\mathbf{F}}_j$ is the force applied by an impact and $\tilde{\mathbf{G}}_j$ is the seismic station’s response function, we require that, over $j \neq k$,

$$\mathbb{E} \left[\left(\tilde{\mathbf{F}}_j \cdot \tilde{\mathbf{G}}_j \right) \left(\tilde{\mathbf{F}}_k \cdot \tilde{\mathbf{G}}_k \right) \right] = 0, \quad (1)$$

where we write \mathbb{E} for the expectation of a random variable. We describe two scenarios in which this will not be true and two methods for ensuring that it is.

First, we note that signals will, in general, be correlated at the low frequencies that correspond to the timescales of variation of the bulk flow. For example, if T is a time interval over which a flow runs into a southern valley wall and turns north, impacts during the turn will apply forces on the bedrock that, averaged over T , are directed southwards more often than northwards. At frequencies less than $1/2T$,

the Fourier transforms of these forces will therefore tend to have the same sense, and so these impacts will - barring large phase differences in a seismic station’s response - generate correlated signals. Similarly, signals will be correlated if impacts occur at regular intervals; a particle undergoing similar impacts at constant time intervals Δt_i will generate, at a seismic station with similar response functions to such impacts, correlated signals from the impacts at all frequencies that are multiples of $1/\Delta t_i$.

In both cases, the correlation can often be avoided by considering the total signal generated by a sufficiently large spatial and temporal extent. If the time over which the frequency-space signal is measured is longer than the time over which impacts are correlated (so that e.g. northwards-directed forces contribute to the total signal as much as southwards-directed ones) and the region considered extends beyond the lengths over which impacts are correlated (so that e.g. the total signal has contributions from other particles with the same Δt_i interval between impacts, but different phases), then correlations between close impacts will be cancelled out by anticorrelations between distant impacts, and the total correlation will be close to zero. However, consideration of larger spatial and temporal extents decreases resolution and makes the mean properties of the flow less representative of the local flow properties that determine individual impacts.

These problems can be avoided by considering the signals at higher frequencies. Informally, high-frequency signals can only be correlated if patterns in impact properties, such as the above examples, hold to an improbably high degree of precision in time. Formally, we can write the Fourier-space signal for the j th impact as $\tilde{v}_j(\omega)e^{-i\omega t_j}$ for angular frequency ω , with t_j the time at which the impact starts and with differences in \tilde{v}_j linked only to differences in the physics governing each impact signal. If, for two impacts, the joint probability distribution of \tilde{v}_j , \tilde{v}_k and $t_j - t_k$ is $f_P(\mathbf{v}, t)$, then the expected correlation between two different signals will be

$$\mathbb{E} \left[\tilde{v}_j^*(\omega) \tilde{v}_k(\omega) e^{i\omega(t_j - t_k)} \right] = \int_{\mathbb{C}^2 \times \mathbb{R}} v_1^* v_2 e^{i\omega t} f_P(\mathbf{v}, t) dv_1 dv_2 dt. \quad (2)$$

Now, we write T for the time over which mean flow properties vary and $\sigma_{\Delta t}$ for the standard deviation of the interval between consecutive correlated impacts. For $\omega \gg 1/\sigma_{\Delta t}$ and $\omega \gg 1/T$, impacts will occur at a constant rate between t and $t + 1/\omega$ and the same physics is expected to apply to each impact, so $f_P(\mathbf{v}, t)$ will vary little over the timescale $1/\omega$. However, $e^{i\omega t}$ will have a mean value of zero over the same timescale, and consequently the integral in (2) will vanish, in the spirit of the Riemann-Lebesgue lemma. Therefore, we expect signals at periods much less than the timescales of flow variation or impact-time co-ordination to be uncorrelated. Such signals will be non-negligible if the duration of impacts is much less than these timescales and this will be the case if the materials involved in an impact are sufficiently stiff.

S2.4. Mean Properties Must Determine Impact Signals

Finally, for some mean properties of the flow to be linked via individual impacts’ properties to the seismic signal observed at a remote station, we require the flow to be divisible into spatial and temporal domains that satisfy two properties. The domains must be a) large enough for the law of large numbers to apply to the signals from individual impacts within them, which can therefore be predicted using mean properties of each flow domain, but b) small enough that there is little variation in the magnitude of the remote station’s response function to those signals, so that the same Green’s function can be used for all such signals. Such domains will exist if the spatial and temporal intervals between impacts are much smaller than the length and time scales of variation of the flow or the Green’s functions for signal propagation.

S3. Hertz Theory

We consider binary, elastic, quasistatic, normal interactions between spheres, which is the axisymmetric case of the problem introduced and solved by Hertz (1881). This is a strong set of assumptions, but we expect the derived results to be reasonable approximations, since the energetic collisions between glass beads which contributed most to the seismic signal exhibit a) short collision durations, so that a binary approximation is not unreasonable; b) restitution coefficients close to one, so that collisions are approximately elastic; c) impact speeds much less than the materials' speeds of sound, so that materials' internal deformation adjusts rapidly to changes of particle positions; and d) low friction coefficients, so that the normal forces between particles are much larger than the tangential forces. For homogeneous spheres with radii r_1 and r_2 , Young's moduli E_1 and E_2 , and Poisson's ratios ν_1 and ν_2 , with centres separated by $r_1 + r_2 - \delta$, Hertz (1881) derives that the normal force between the particles is

$$F_n = \kappa \delta^{3/2}, \quad (3)$$

for κ related to harmonic means of the particles' properties by

$$\kappa = \frac{4}{3} \left(\frac{1 - \nu_1^2}{E_1} + \frac{1 - \nu_2^2}{E_2} \right)^{-1} \sqrt{\left(\frac{1}{r_1} + \frac{1}{r_2} \right)^{-1}}. \quad (4)$$

If the first particle has density ρ , the second particle is fixed, and the initial normal impact velocity is u_n , then δ satisfies for $m = 4\pi\rho r_1^3/3$ the Newtonian system of equations

$$\begin{aligned} \delta(0) &= 0, \\ \dot{\delta}(0) &= u_n, \\ m\ddot{\delta}(t) &= -\kappa\delta(t)^{3/2}. \end{aligned} \quad (5)$$

Noting that we have three parameters κ , m , and u_n in the three dimensions mass, length, and time, we can by the Buckingham π theorem (Bertrand, 1878; Buckingham,

1914) define typical length and time scales for the impact

$$\begin{aligned} \lambda &= \left(\frac{mu_n^2}{\kappa} \right)^{2/5} \\ &= \left[\pi^2 \rho^2 u_n^4 \left(\frac{1 - \nu_1^2}{E_1} + \frac{1 - \nu_2^2}{E_2} \right)^2 \left(1 + \frac{r_1}{r_2} \right) \right]^{1/5} r_1, \end{aligned} \quad (6)$$

$$\begin{aligned} \tau &= \left(\frac{m^2}{\kappa^2 u_n} \right)^{1/5} \\ &= \left[\frac{\pi^2 \rho^2}{u_n} \left(\frac{1 - \nu_1^2}{E_1} + \frac{1 - \nu_2^2}{E_2} \right)^2 \left(1 + \frac{r_1}{r_2} \right) \right]^{1/5} r_1, \end{aligned} \quad (7)$$

and can switch to a non-dimensional system of equations for $\Delta = \delta/\lambda$ as a function of $T = t/\tau$:

$$\begin{aligned} \Delta(0) &= 0, \\ \Delta'(0) &= 1, \\ \Delta''(T) &= -\Delta(T)^{3/2}. \end{aligned} \quad (8)$$

We solve these equations numerically, with Figure S1a indicating the evolution over time of the non-dimensional normal deformation Δ and force $\mathcal{F}_n = F_n/\kappa\lambda^{3/2}$, and Figure S1b showing the power spectrum $|\tilde{\mathcal{F}}_n|^2$ of that non-dimensional normal force.

We note that since the impact is elastic and of finite duration, the first particle's non-dimensional post-impact velocity is $\lim_{T \rightarrow \infty} \Delta'(T) = -1$, and so the zero-frequency limit of the basal force's Fourier spectrum is

$$\begin{aligned} \tilde{\mathcal{F}}_n(0) &= \int_{-\infty}^{\infty} -\Delta''(T) dT \\ &= 2. \end{aligned} \quad (9)$$

We therefore define a non-dimensional function $\zeta(f\tau) = |\tilde{\mathcal{F}}_n(f\tau)|^2/4$, and note from the numerical solution (or else by the integrability, non-negativity, and symmetry of \mathcal{F}_n) that ζ is approximately equal to 1 for $f\tau \ll 1$, monotonically decreases to $\zeta(f_c\tau) = 0.5$ for a non-dimensional corner frequency that we calculate to be approximately $f_c\tau = 0.208$, and is much less than 1 for $f\tau > 1$.

Re-dimensionalising, we note that the spectral density of the normal force has units $\text{kg}^2 \text{m}^2 \text{s}^{-2}$ and so that

$$|\tilde{F}_n(f)|^2 = (mu_n)^2 |\tilde{\mathcal{F}}_n(f\tau)|^2 = \left(\frac{\pi \rho d^3 u_n}{3} \right)^2 \zeta(f\tau), \quad (10)$$

while for beads with equal diameters d , Young's moduli E , and Poisson's ratios ν ,

$$\tau = \left[\frac{\pi^2 \rho^2 (1 - \nu^2)^2}{4E^2 u_n} \right]^{1/5} d. \quad (11)$$

For disparate particles, as in section S7.3, we can re-dimensionalise using mass m and the length and time scales defined in equations (6) and (7).

S4. Amplifier Settings

Before the first experiment, we uploaded settings for the Kistler 5073 charge amplifier via an RS232 interface with the laboratory laptop, using the Python program `kistler_control.py` in the GitLab repository for this paper (Arran et al., 2021). With this program, we set the amplifier sensitivity to its maximal value of 0.1 V pC^{-1} and the amplifier bandwidth filter was turned off.

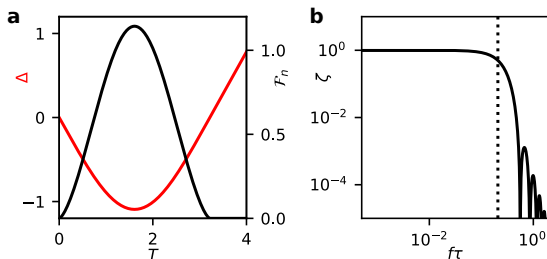


Figure S1. *Non-dimensional evolution of a Hertzian impact.* a) Evolution of the normal deformation Δ (red) and normal force \mathcal{F}_n (black). b) Shape function ζ for the power spectral density $|\tilde{\mathcal{F}}_n|^2 = 4\zeta$ of normal force, with the corner frequency $f_c\tau$ indicated (dotted line).

For each channel inclination and reservoir gate height, we set the settings of the Brüel and Kjær Nexus 2692-A-OS4 conditioning amplifier using its manual user interface. The nominal sensitivity of the accelerometers was set to $s_a = 0.006 \text{ pC} / (\text{m s}^{-2})$ and the nominal sensitivity of the amplifier to the highest value s_A among 3.16, 10, and $31.6 \text{ mV} / (\text{m s}^{-2})$ for which the amplifier's output remained below 10 V. We define $A = s_A / s_a$ for the true amplification. We set the corner frequencies of the amplifier's bandpass filter to their minimal and maximal values, respectively, of 10 Hz and 100 kHz.

S5. Experiment Control

We used a variety of programs to control the experiment and record data. At each channel inclination and release gate height, the program `run_experiment.ino` was uploaded to the microcontroller, with a defined experiment duration T_e , camera delay T_d , and camera footage duration T_c . Then, before each experiment, three programs started running in order to record data: Optronis' TimeViewer software to record camera footage at frame rate 2 kHz, subject to an external trigger and over duration T_c ; the program `record_picoscope.exe` to record data from the oscilloscope at sample rate 250 kHz, with an external trigger and duration T_e set by settings file `exp_settings.txt`; and the program `record_balance.py` to record data from the mass balance at 5 Hz and over duration T_e , starting after a three-second beeped countdown and a 'go' beep. All programs are available on a GitLab repository associated with this paper (Arran et al., 2021).

Signals sent between the apparatus synchronised measurements. The `record_balance.py` program emitted a 'go' beep to mark the start of the experiment, upon which the experimentalist manually lifted the reservoir's release gate and pressed a start switch. This switch completed a circuit, increasing the voltage at the Arduino microcontroller's analogue input pin. The microcontroller responded by sending a digital signal to the force sensor amplifier and to the oscilloscope, and by starting a delay timer of duration T_d . In turn, the force sensor amplifier responded to the signal by switching to 'Measure' mode, amplifying the plate-normal, downslope, and cross-slope signals from the force sensor and transmitting them to the oscilloscope, for which the microcontroller's signal was the external trigger to start recording the signals from both the force sensor amplifier and the accelerometer amplifier, sending them to the Lenovo laptop. While the oscilloscope was recording data, the microcontroller reached the end of its time delay T_d and sent a digital signal to switch a relay, which in turn sent a trigger signal to the high-speed camera to initiate its recording, with data again sent to the laptop. Figure S2 is a schematic of this control system.

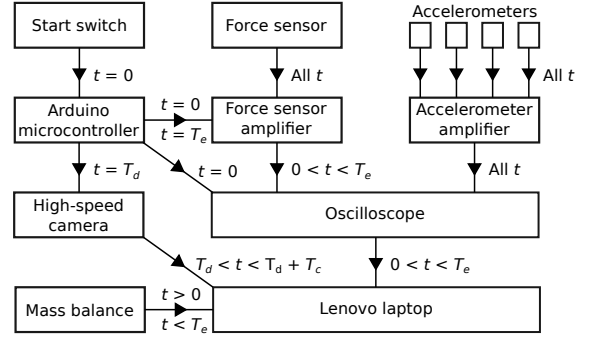


Figure S2. Schematic of experimental control and measurement system. The experiment is controlled and measurements recorded via signals sent between the labelled devices. Arrows indicate the signals sent between devices, with labels indicating the times at which they are sent.

S6. Calculation of the Net Force on the Instrumented Plate

Here, we describe our derivation, calibration, and validation of a relation between a) the net force applied by the flow to the instrumented plate, and b) the voltage outputs of the force sensor's charge amplifier.

S6.1. Derivation

The three voltage outputs from the force sensor's charge amplifier, after being downsampled to 200 Hz by averaging over 5 ms intervals, were each the sum of three components: a zero offset following the switch to the 'Measure' mode; an approximately linear drift over time due to charge build-up; and a signal from the sensor that was linear in the forces applied to the plate by the flow, but with cross-talk between the different components of force and with unknown coefficients. Writing the downsampled voltage and force as $\mathbf{V}(t)$ and $\mathbf{F}(t)$, there existed varying offset and drift vectors \mathbf{V}^0 and α , and a constant response matrix β , such that

$$\mathbf{V}(t) \approx \mathbf{V}^0 + \alpha t + \beta \mathbf{F}(t). \quad (12)$$

To recover the downslope and plate-normal forces applied to the plate, under the assumption that the contribution of the cross-slope force was negligible, we considered the two corresponding voltage outputs; directly removed the effect of the zero offset \mathbf{V}^0 ; subtracted the expected linear drift $\mathbb{E}[\hat{\alpha}]t$, as calibrated from preliminary measurements; and multiplied by the inverse of the relevant 2-by-2 response sub-matrix $\hat{\beta}$, as calibrated from measurements taken between experiments. Specifically, we took

$$\mathbf{F}(t) = \hat{\beta}^{-1} [\mathbf{V}(t) - \mathbf{V}(t_0) - \mathbb{E}[\hat{\alpha}](t - t_0)], \quad (13)$$

with $t_0 = 0.8 \text{ s}$, at which time the zero offset had stabilised and there was no external force on the instrumented plate, and with estimates for $\mathbb{E}[\hat{\alpha}]$ and $\hat{\beta}$ from calibration.

S6.2. Calibration

To estimate the mean drift vector $\mathbb{E}[\hat{\alpha}]$, we took 10 zero-load recordings, for each of which the force sensor's output was recorded over 110 s with no external force on the instrumented plate. Dividing by 100 the change in V_j over the 100 s after t_0 , we calculated the $\hat{\alpha}$ for each recording, and recovered

$$\mathbb{E}[\hat{\alpha}_x] = (121 \pm 7) \mu\text{V s}^{-1} \text{ and } \mathbb{E}[\hat{\alpha}_z] = (225 \pm 18) \mu\text{V s}^{-1}, \quad (14)$$

with each error being the standard error in the sample mean, as described in S9.

To estimate the response matrix $\hat{\beta}$, we took four static-load recordings before each set of experiments at a given channel incline $\tan \theta$ and release gate height h_g , and four after. For each recording, we attached a cradle to the centre of the instrumented plate with double-sided tape, then recorded the force sensor's output over 5 s, adding to the cradle, 1 s to 2 s after starting, 10 metal plates with combined mass $M_c = 442.3$ g. Calculating, for each recording, over all t between 3 s and 4 s, the average voltage response $\mathbf{V}^r = (\mathbf{V}(t) - \mathbf{V}(t_0) - \mathbb{E}[\hat{\alpha}](t - t_0))_{\Delta t}$, we calculated over all such \mathbf{V}^r the least-squares best-fit matrix $\hat{\beta}$ for the linear model $\mathbf{V}^r = \hat{\beta} M_c g (\sin \theta, \cos \theta)$, with gravity $g = 9.81 \text{ m s}^{-2}$. The result was

$$\begin{pmatrix} \hat{\beta}_{xx} & \hat{\beta}_{xz} \\ \hat{\beta}_{zx} & \hat{\beta}_{zz} \end{pmatrix} = \begin{pmatrix} 0.83102 & -0.03522 \\ -0.13462 & 0.35345 \end{pmatrix} \text{V N}^{-1}, \quad (15)$$

with the fit achieved by the linear model plotted in Figure S3.

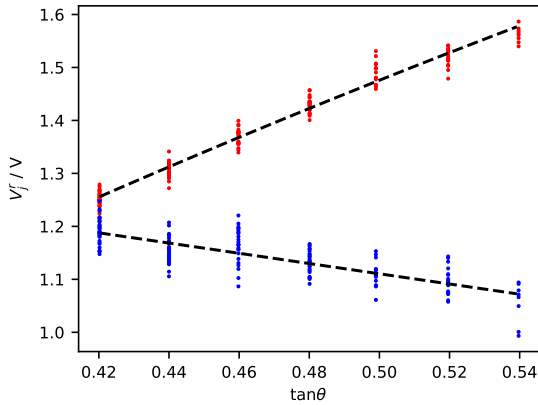


Figure S3. The force sensor's response to static loads. Points represent the voltage response of the downslope (red) and plate-normal (blue) outputs of the force sensor's charge amplifier, to an $M_c g = 4.34 \text{ N}$ vertical load on the plate's centre, at different channel inclines $\tan \theta$. Lines represent the theoretical response, for a best-fit response matrix $\hat{\beta}$. Scatter arises from variations in $\hat{\alpha}$ from its expected value and from imperfections in the centering of the load.

S6.3. Validation

Since the measured effective friction on the plate μ is the ratio of time averages of the two inferred force components, it is particularly sensitive to this calibration, so we performed tests to validate the use of equation (13) and of the above values of $\mathbb{E}[\hat{\alpha}]$ and $\hat{\beta}$.

To test the measurement of the static friction between a volume of glass beads and the instrumented plate, we closed off the channel at its end and filled it with beads, recording the force sensor's voltage response to the resulting static load and calculating μ . To reduce the effect of $\hat{\alpha}$'s variability around its expected value, we repeated this measurement of μ three times and took the average, at each of a range of channel inclines θ between 15° and 25° . The resulting averages agreed with the theoretical values $\tan \theta$ to within both two mean standard errors and 10%.

To test the measurement of dynamic friction, we released weighted sledges from rest at the top of the instrumented plate, inferring their accelerations from high-speed-camera

footage and comparing the implied friction coefficients between the sledges and the plate to those measured with the force sensor. If $\hat{\mu}$ is the true, constant friction coefficient between a sledge and the plate, it will be linked to the time T for the front of the sledge to cross the instrumented plate by $X = g(\sin \theta - \hat{\mu} \cos \theta)T^2/2$, so we manually extracted T from the camera footage, calculated the implied value of $\hat{\mu}$, and compared it to the effective friction measured over the 4 s after t_0 . We repeated the test three times for each of three sledges, with bases of printer paper, plastic mesh, and wetted tissue paper, and corresponding implied friction coefficients $\hat{\mu} = 0.227 \pm 0.002$, 0.340 ± 0.008 , and 0.468 ± 0.010 , released at channel inclines $\tan \theta = 0.3648$, 0.5609 , and 0.6852 , respectively, and in each case the average value of μ agreed with $\hat{\mu}$ to within two mean standard errors and 15%, despite significant variation of the instantaneous value of F_x/F_z .

S7. Calculation of the Power Spectrum of the Basal Force Applied by the Flow

Here, we describe our derivation, calibration, and validation of a relation between a) the power spectrum of the basal force applied by the flow to the instrumented plate, and b) the measurements of the accelerometers on the bottom of the plate.

S7.1. Derivation

To derive such a relation, we consider the deformation of the instrumented plate in response to a single impact's force; calculate the contribution of that response to the mean seismic energy within the plate; consider the total mean seismic energy, due to multiple impacts; and link that energy to the measurements of accelerometers.

Since the steel structure of the plate is thin, stiff, and elastic, we may assume that linear Kirchhoff-Love plate theory applies in calculation of its deformation (Love & Darwin, 1888; Ciarlet, 1997). We further assume isotropy and homogeneity of the steel. Writing ρ_p , E_p , ν_p , X , Y , and H for the steel's density, Young's modulus, Poisson's ratio, length, width, and thickness, and defining its bending stiffness $D = E_p H^3 / 12(1 - \nu_p^2)$, then its normal displacement w satisfies

$$D \nabla^2 \nabla^2 w = -\rho_p H \partial_t^2 w + p, \quad (16)$$

for p the normal force per unit area to which the plate is subject. The relevant boundary conditions in our case are a clamped centre and free edges forming a rectangle. Now, on the set of functions satisfying these conditions, the left-hand-side operator in equation (16) is self-adjoint, so that we may define an orthonormal basis of eigenfunctions $\psi_j(\mathbf{x})$ with corresponding positive, real eigenvalues $4\pi^2 \rho_p H f_j^2$, and may write $w_j(t)$ for the components of w with respect to this basis. Substituting into equation (16), the orthonormality of the basis functions allows us to recover the ordinary differential equation

$$\left(\frac{d^2}{dt^2} + 4\pi^2 f_j^2 \right) w_j = \frac{1}{\rho_p h X Y} \int_{XY} \psi_j p \, d^2 \mathbf{x}. \quad (17)$$

If we impose $w = 0$ for $t < -T$, and suppose p represents an impact, so is a point force at \mathbf{x}_0 with support $[-T, 0]$, then we can solve this equation using the Green's function for the left-hand differential operator, $G(t; \tau) = \sin(2\pi f_j[t - \tau]) / 2\pi f_j$. Writing $p(\mathbf{x}, t) = \delta(\mathbf{x} - \mathbf{x}_0) F_i(t)$ for Dirac delta function δ and plate-normal impact force F_i , and writing the sine function as a sum of exponentials, we recover that for $t > 0$

$$\begin{aligned} w_j(t) &= \int_{-\infty}^t \frac{\psi_j(\mathbf{x}_0)}{4\pi i \rho_p H X Y f_j} \left(e^{2\pi i f_j(t-\tau)} - e^{-2\pi i f_j(t-\tau)} \right) F_i(\tau) \, d\tau \\ &= \frac{\psi_j(\mathbf{x}_0)}{2\pi \rho_p H X Y f_j} \Im \left[e^{2\pi i f_j t} \tilde{F}_i(f_j) \right], \end{aligned} \quad (18)$$

where $\tilde{\cdot}$ denotes a Fourier transform and $\Im[\cdot]$ the imaginary component, and we assume that F_i is real, so that $\tilde{F}_i(-f) = \tilde{F}_i(f)^*$.

We calculate the expected contribution of this response to the plate's mean seismic energy by assuming that the impacts are equally likely anywhere on the plate, and that energy is linearly attenuated, with quality factor $Q \gg 1$. We note that each eigenfunction component $w_j\psi_j$ behaves like a simple harmonic oscillator and that the eigenfunctions' orthogonality allows the energy of each component to be considered separately. Therefore, writing $\langle \cdot \rangle_{1/f_j}$ for time averages over the modes' cycles, the expected mean seismic energy in the plate, per unit area, due to the impact and immediately after it, will be

$$\begin{aligned} \mathcal{E}_i(0) &= \frac{1}{X^2Y^2} \int_{XY} d\mathbf{x}_0 \int_{XY} d\mathbf{x} \sum_j \rho_p H \langle \dot{w}_j^2 \psi_j^2 \rangle_{1/f_j} \\ &= \sum_j \frac{|\tilde{F}_i(f_j)|^2}{2\rho_p H X^2 Y^2}, \end{aligned} \quad (19)$$

where again we have used the orthonormality of the basis functions. Linear attenuation will result in the exponential decay of this energy over time, with the j th mode's contribution having decay constant $2\pi f_j/Q$. For any time interval Δt starting before $t = 0$ and lasting until $t \gg Q/2\pi \min(f_j)$, the mean seismic energy in the plate over this time interval will therefore be

$$\langle \mathcal{E}_i \rangle_{\Delta t} \approx \sum_j \frac{Q |\tilde{F}_i(f_j)|^2}{4\pi \rho_p H X^2 Y^2 f_j \Delta t}. \quad (20)$$

We note that only for $f_j T > Q/2\pi$ will a) attenuation affect the response during the interval $[-T, 0]$, and b) this interval be significant in the averaging, and we ignore such high frequencies, at which $|\tilde{F}_i(f_j)|^2$ will be negligible: for a Hertzian impact with $Q = 100$, $f_j T > Q/2\pi$ implies that $|\tilde{F}_i(f_j)|^2 / |\tilde{F}_i(0)|^2 < 10^{-9}$.

To consider the plate's total energy rather than the contributions of individual impacts, we also restrict our attention to frequencies at which both individual impacts' forces and the responses to those forces are uncorrelated, as discussed in S2. Consequently, we can relate the total normal force on the plate F and the plate's total energy per unit area \mathcal{E} , over time Δt , to the contributions F_i and \mathcal{E}_i of individual impacts within Δt :

$$|\tilde{F}(f)|^2 = \sum_i |\tilde{F}_i(f)|^2, \quad \langle \mathcal{E} \rangle_{\Delta t} = \sum_i \langle \mathcal{E}_i \rangle_{\Delta t}, \quad (21)$$

with cross terms making no net contribution and Fourier transforms taken over Δt . We can therefore sum equation (20) over all impacts to recover an expression for the plate's total energy in terms of the power spectrum $|\tilde{F}(f)|^2$ of the total force applied on the plate.

To link this power spectrum $|\tilde{F}(f)|^2$ to the measured vertical acceleration of the plate's steel structure, we assume that a) a proportion \mathcal{P} of the plate's energy is associated with the steel's vertical deformation and b) $|\tilde{F}(f)|$ varies sufficiently slowly that we can estimate its values away from the plate's resonant frequencies f_j . The relevant frequency scale is the mean bandgap between eigenvalues of equation (16) in the case of simply supported boundaries, for which the eigenfunctions $\hat{\psi}_{jk}$ and eigenvalues \hat{f}_{jk} are

$$\hat{\psi}_{jk}(x, y) = 4 \sin\left(\frac{j\pi x}{X}\right) \sin\left(\frac{k\pi y}{Y}\right), \quad (22)$$

$$\hat{f}_{jk} = \frac{\pi}{2} \left(\frac{j^2}{X^2} + \frac{k^2}{Y^2} \right) \sqrt{\frac{D}{\rho_p H}}. \quad (23)$$

Noting that the number of eigenvalues less than $\pi R^2 \sqrt{D}/2 \sqrt{\rho_p H}$ may be approximated by the area of a quarter-ellipse with major and minor axes XR and YR , this mean bandgap is

$$\Delta_f = \frac{2}{XY} \sqrt{\frac{D}{\rho_p H}}, \quad (24)$$

which will be equal to the corresponding asymptotic mean bandgap of the eigenvalues f_j for our problem, on the same domain. We use this to approximate the discrete spectrum on the right-hand side of equation (20) with a continuous spectrum; we approximate the left-hand side's mean seismic energy $\langle \mathcal{E} \rangle_{\Delta t}$ using a moving average $\langle |\tilde{a}(f)|^2 \rangle_{\Delta f}$, over a frequency scale $\Delta f \gg \Delta_f$, of the mean spectral density of the steel's vertical acceleration. Recalling that the vertical acceleration accounts for only a proportion \mathcal{P} of the total energy, we recover

$$\frac{1}{\mathcal{P} \Delta t} \int_{-\infty}^{\infty} \rho_p H \frac{\langle |\tilde{a}(f)|^2 \rangle_{\Delta f}}{(2\pi f)^2} df \approx \int_0^{\infty} \frac{Q |\tilde{F}(f)|^2}{4\pi \rho_p H X^2 Y^2 f \Delta_f \Delta t} df, \quad (25)$$

for both Fourier transforms restricted to the interval Δt . Consequently, noting that $a(t)$ is real and so $|\tilde{a}(f)|^2$ is symmetric, and approximating its value with the measurements a_k of the four accelerometers, our estimate of the power spectrum of the basal force applied by the flow to the instrumented plate is

$$P_F(f) = \frac{|\tilde{F}(f)|^2}{\Delta t} \approx \frac{(\rho_p H)^{3/2} XY \sqrt{D}}{\pi \mathcal{P} Q f \Delta t} \left(\sum_{k=1}^4 |\tilde{a}_k(f)|^2 \right)_{\Delta f}. \quad (26)$$

With the accelerometers' calibrated sensitivities s_k taken from their calibration sheets, and the accelerometers' conditioning amplifier having amplification A , as defined in S4, the power spectral densities $|\tilde{a}_k|^2$ of the measured accelerations were calculated from the amplifier's output voltages V_k as

$$|\tilde{a}_k(f)|^2 = \frac{\Gamma(f)}{(A s_k)^2} |\tilde{V}_k(f)|^2, \quad (27)$$

where $\Gamma(f) = 1 + (f/f_M)^n$ is a high-frequency correction for the accelerometers' non-constant frequency response and for the amplifier band-pass filter mentioned in S4, with f_M and n determined by the calibration described in section S7.3.

S7.2. Calibration

To calibrate the values of \mathcal{P} and Q , and to extend the frequency range in which $|\tilde{a}_k|^2$ could be measured correctly, by calibrating f_M and n in Γ , we used the impacts of individual 2-mm-diameter glass beads, dropped onto random positions on the instrumented plate from a height of $h_i = 1$ m, with the channel inclined at $\theta = 0^\circ$. The use of ball impacts to calibrate sensors is suggested in e.g. McLaskey and Glaser (2010), and allows calibration over frequency and force scales directly relevant to our experiments.

To record and analyse data, we used automatic triggers to record the voltage outputs of the accelerometers' conditioning amplifier throughout and after each of 25 impacts, at 250 kHz over 0.06 s, with amplification $A = 1.67$ V pC $^{-1}$. We divided these voltages by A and by the accelerometers' documented sensitivities $s_1 = 6.75$ fC/(ms $^{-2}$), $s_2 = 5.61$ fC/(ms $^{-2}$), $s_3 = 5.38$ fC/(ms $^{-2}$), and $s_4 = 6.58$ fC/(ms $^{-2}$), to recover the band-pass-filtered acceleration measurements $\hat{a}_k(t)$. To consider individual frequency components of these accelerations at maximum precision in both the frequency and time domains, we calculated their wavelet transforms using unit Gabor wavelets with centre

frequencies f_0 between 256 Hz and 125 kHz and standard deviations in frequency space $\sigma_{f_0} = f_0/4\pi$:

$$\mathcal{W}[\hat{a}_k](f_0, t_0) = \left(\frac{f_0^2}{2\pi}\right)^{1/4} \int_{-\infty}^{\infty} \hat{a}_k(t) e^{-\frac{f_0^2(t-t_0)^2}{4}} e^{2\pi i f_0(t-t_0)} dt. \quad (28)$$

We then calculated the corresponding spectral density, locally averaged around each f_0 , of the plate's steel structure's vertical-displacement-associated seismic energy per unit area:

$$\hat{\Psi}_{f_0}(t) = \frac{1}{4} \sum_{k=1}^4 \frac{\rho_p H |\mathcal{W}[\hat{a}_k](f_0, t)|^2}{(2\pi f_0)^2}, \quad (29)$$

for $\rho_p = 7800 \text{ kg m}^{-3}$ and $H = 2 \text{ mm}$. To extract the energy spectral density $\hat{\Psi}_{f_0}^0$ immediately after each impact, and the decay rate k_{f_0} of the spectral density over time, we performed a linear regression of $\ln \hat{\Psi}_{f_0}$ against t , over the time following the impact for which the signal was above the level of noise. An example for a single impact and wavelet is shown in Figure S4a, while Figure S4b shows the resulting average decay rates $\langle k_{f_0} \rangle$, over all 25 impacts, and Figure S4c shows the similarly averaged post-impact energy spectral densities $\langle \hat{\Psi}_{f_0}^0 \rangle$.

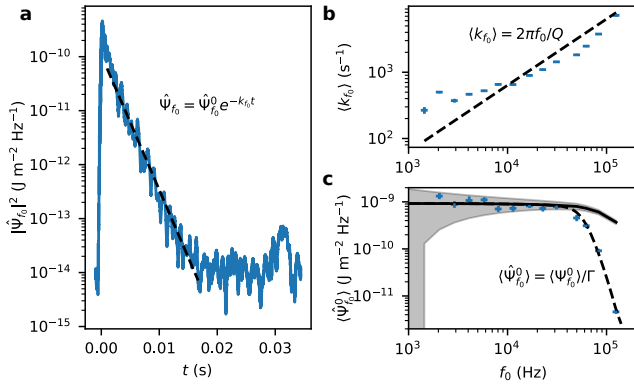


Figure S4. The accelerometers' response to individual impacts of glass beads. a) The plate's steel structure's vertical-displacement-associated seismic energy density $\hat{\Psi}_{f_0}$, localised around $f_0 = 8.1 \text{ kHz}$, as inferred from uncalibrated accelerometer measurements for a single impact, decays exponentially. The dashed line indicates the linear regression of $\ln \hat{\Psi}_{f_0}$ against t , allowing extraction of the post-impact energy spectral density $\hat{\Psi}_{f_0}^0$, and the decay rate k_{f_0} . b) Points represent the mean decay rates $\langle k_{f_0} \rangle$ over 25 impacts. The dashed line indicates the theoretical relation, for best-fit quality factor Q . c) Points represent the mean measured post-impact energy spectral densities $\langle \hat{\Psi}_{f_0}^0 \rangle$, over 25 impacts. The solid line indicates the theoretical value $\langle \hat{\Psi}_{f_0}^0 \rangle$ for a flat accelerometer response and for fitted $\mathcal{P} = 0.25$; the solid area its theoretical standard error; and the dashed line the theoretical relation for the best-fit high-frequency response correction $\Gamma(f) = 1 + (f/f_M)^n$. In both b and c, vertical and horizontal errorbars indicate the mean standard error over different impacts and the wavelet standard deviation in frequency space, respectively.

We used these data to perform the calibration, recovering the quality factor $Q = 99 \pm 12$ as the mean of $2\pi f_0 / \langle k_{f_0} \rangle$,

and calibrating \mathcal{P} , f_M and n by comparing the measured values $\langle \hat{\Psi}_{f_0}^0 \rangle$ to the theoretical values of the plate's total post-impact energy spectral density $\langle \Psi_{f_0}^0 \rangle / \mathcal{P}$ predicted by equation (19) and the Hertz theory described in S3. Specifically, we noted that each dropped glass bead impacted, vertically, a glass bead attached to the plate in an approximately hexagonal packing, and we calculated the resulting random distribution of the angle θ_i between the vertical and the normal between impacted and impacting beads. To simulate an impact, we pulled θ_i from this distribution and took the spectral density of the applied plate-normal force to be

$$|\tilde{F}(f)|^2 = |\tilde{F}_n(f; \cos \theta_i \sqrt{2gh_i})|^2 \cos^2 \theta_i, \quad (30)$$

for $F_n(t; u_n)$ the Hertzian normal force between two spheres colliding at normal velocity u_n and with the glass beads' material properties: density $\rho = 2500 \text{ kg m}^{-3}$, diameter $d = 2 \text{ mm}$, Young's modulus $E = 63 \text{ GPa}$, and Poisson's ratio $\nu = 0.23$. By S3, this spectral density varies over frequency scales $\hat{f}_c/\tau \approx 100 \text{ kHz} \gg \sigma_{f_0}$, so equation (19) implies that the impact imparts energy with expected spectral density around f_0

$$\frac{\Psi_{f_0}^0}{\mathcal{P}} \approx \frac{|\tilde{F}(f_0)|^2}{4\rho_p H X^2 Y^2 \Delta_f}, \quad (31)$$

for mean bandgap Δ_f given by equation (24) using the steel structure's material properties: density $\rho_p = 7800 \text{ kg m}^{-3}$, length $X = 0.18 \text{ m}$, width $Y = 0.1 \text{ m}$, thickness $H = 2 \text{ mm}$, and bending stiffness $D = E_p H^3 / 12(1 - \nu_p^2)$ for Young's modulus $E_p = 200 \text{ GPa}$ and Poisson's ratio $\nu_p = 0.29$. We calculated $\langle \Psi_{f_0}^0 \rangle / \mathcal{P}$ as the average of $\Psi_{f_0}^0 / \mathcal{P}$ over 25 simulated impacts, and noted that the dominant source of systematic error in its value was the varying number of resonant frequencies in each wavelet's frequency range, approximated as the 95% confidence interval $f_0 \pm 2\sigma_{f_0}$. We therefore estimated the error by supposing this number had a Poisson distribution with mean $4\sigma_{f_0} / \Delta_f$. Finally, we calculated $\mathcal{P} = 0.25$ for consistency between measured $\langle \hat{\Psi}_{f_0}^0 \rangle$ and theoretical $\langle \Psi_{f_0}^0 \rangle$ at low f_0 , and the least-squares best-fit values $f_M = 60 \text{ kHz}$ and $n = 6$ for the correction to the high-frequency response of the accelerometers and accelerometer amplifier:

$$\langle \Psi_{f_0}^0 \rangle / \langle \hat{\Psi}_{f_0}^0 \rangle = \Gamma(f_0) = 1 + (f_0/f_M)^\alpha. \quad (32)$$

S7.3. Validation

We performed a different set of impact experiments to verify 1) the acoustic isolation of the instrumented plate from the rest of the channel - that only impacts on the plate made significant contributions to its normal displacement - and 2) the validity of equation (26) for the vertical basal force's spectral density $|\tilde{F}|^2$, with equation (27) for the measured accelerations and with $\mathcal{P} = 0.25$, $Q = 99$, $f_M = 60 \text{ kHz}$, and $n = 6$. With the channel flat, we dropped steel ball bearings of diameter $(3.125 \pm 0.007) \text{ mm}$ from a metal plate $(100.68 \pm 0.02) \text{ mm}$ above the channel bed, onto a) 10 random positions on the plate, and b) 10 random positions off the plate, 10 mm from its edge. Having used automatic triggers to record the voltage output of the accelerometers' conditioning amplifier throughout and after the impact, at 250 kHz over 0.04 s, with amplification $A = 0.527 \text{ V pC}^{-1}$ in case a and 16.7 V pC^{-1} in case b, we calculated in each case the inferred spectral density $|\tilde{F}|^2$ of the basal force. This is plotted, and in case a compared to its theoretical value, in Figure S5.

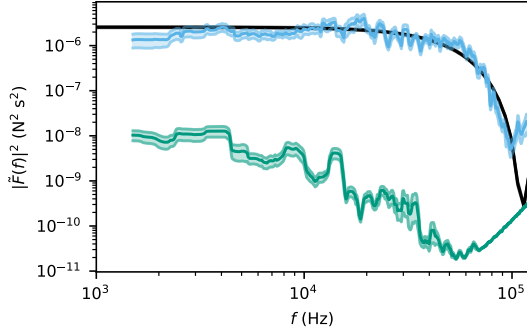


Figure S5. *The inferred spectrum of the vertical basal force applied by a ball bearing's impact. Using appropriate material parameters and calibrated \mathcal{P} , Q , f_M and n , the spectral density calculated using equations (26) and (27) for an on-plate impact (blue) is consistent with the theoretical spectral density (black) at all frequencies at which the accelerometers' signal is distinguishable from noise. Under the same conditions, the contributions from an off-plate impact (green) are less than 1 % of those from an on-plate impact. All error regions represent the mean standard errors over different impacts.*

Figure S5 shows that 1) the plate is acoustically isolated from the rest of the channel, and 2) equations (26) and (27) are valid for $\mathcal{P} = 0.25$, $Q = 99$, $f_M = 60$ kHz, and $n = 6$. The contributions of off-plate impacts to $|\tilde{F}|^2$ are less than 1 % of the contributions of on-plate impacts, and the values of $|\tilde{F}|^2$ inferred using sections S7.1 and S7.2 are consistent with the theoretical values $|\tilde{F}_H|^2$, calculated using the Hertz theory that is described in S3, for the impact of a spherical steel ball bearing ($\rho_1 = 7800 \text{ kg m}^{-3}$, $d_1 = 3.125 \text{ mm}$, $E_1 = 200 \text{ GPa}$, $\nu_1 = 0.29$) on a spherical glass bead ($\rho_2 = 2500 \text{ kg m}^{-3}$, $d_2 = 2 \text{ mm}$, $E_2 = 63 \text{ GPa}$, $\nu_2 = 0.23$), with impact normal an angle θ_i from the vertical (taken from a random distribution for uniformly distributed impacts of a d_1 -diameter particle on a hexagonal packing of d_2 -diameter particles) and normal velocity $\cos \theta_i \sqrt{2gh_i}$ (for gravitational acceleration $g = 9.81 \text{ m s}^{-2}$ and drop height $h_i = 0.1 \text{ m}$). Discrepancies between theory and observations indicate systematic relative error, due to errors in our attenuation model and variability in the density of the plate's resonant frequencies, which can be estimated as $|\tilde{F}|^2/|\tilde{F}_H|^2 - 1$.

S8. Sidewall Image Processing

To extract profiles of the flow's kinematic properties at the channel wall, we performed five stages of image processing: calibration, particle detection, particle tracking, velocity smoothing, and coarse graining.

Firstly, at each channel incline $\tan \theta$, following camera alignment, we calibrated distances on camera images by capturing an image of a calibration sheet, attached to the inside of the channel wall and covered with a 10 mm chequered pattern. We convolved the greyscale image matrix with an ideal corner pattern; identified corner locations as the weighted centroids of above-threshold regions of the convolution product; and calculated the mean number of pixels between corners horizontally and vertically to determine the correspondence between distances on the channel wall and in its images. The inferred resolution was approximately 8 px mm^{-1} .

Secondly, within each image captured during steady flow, we identified the locations of particles by convolving the greyscale image matrix with a 'typical' particle pattern from a calibration image. The pattern was selected by hand-labelling 25 particles in one image at each channel inclination, and taking the average of their 18×18 greyscale image

matrices. Each peak of the Gaussian-smoothed convolution product was taken to correspond to a particle, located at the local peak of the unsmoothed convolution product. We achieved sub-pixel resolution by fitting Gaussian curves to the local horizontal and vertical variation of the convolution product, about the pixel-resolution peak. This method identified the correct locations of around 90 % of particles visible at the channel wall, robust to specular reflections and variations in lighting.

Thirdly, we tracked particles from one frame to the next by associating each particle identified in each image with the closest particle identified in the previous image, under the conditions that a) the association was not many-to-one, with closer particles having priority, and b) the implied velocity was lower than a 1.2 m s^{-1} limit. This velocity limit corresponded to displacement per frame of one third of a particle diameter, and was more than two standard deviations above the root mean square particle velocity even for the fastest flows.

Fourthly, for each tracked particle, we adjusted for the effect of varying specular reflections on its location estimates, by smoothing the particle velocity over a moving, five-frame window, using a robust weighted least-squares local linear regression. The use of sub-pixel location estimation permitted the use of the robust method, assigning lower weight to outliers, while the linear regression corresponded to finding the best-fit constant acceleration within each 2.5 ms window.

Finally, we used coarse-graining to infer continuum profiles from the point distributions of particle velocities. From the particles' base-normal positions z_j and smoothed velocities \mathbf{u}_j , we estimated the downslope-averaged and time-averaged base-normal profiles, at the channel's wall, of relative volume fraction $\phi_w(z)$, mean velocity $\mathbf{u}_w(z)$, and granular temperature $T_w(z)$ as

$$\phi_w(z) = \langle \sum_j C(z_j; z) \pi d^2 / 4 \rangle_{\Delta t_c} \quad (33)$$

$$\mathbf{u}_w(z) = \langle \sum_j C(z_j; z) \pi d^2 \mathbf{u}_j / 4 \rangle_{\Delta t_c} / \phi_w(z) \quad (34)$$

$$T_w(z) = \langle \sum_j C(z_j; z) \pi d^2 \|\mathbf{u}_j - \mathbf{u}(z)\|^2 / 4 \rangle_{\Delta t_c} / \phi_w(z) \quad (35)$$

for averages $\langle \cdot \rangle_{\Delta t_c}$ over all frames recorded by the camera, sums $\sum_j \cdot$ over all particles detected in each frame, and weighting function C localised around z , with integral over the total spatial domain equal to 1. This process is discussed for general C in Babic (1997), but we took Gaussian profiles

$$C(z'; z) = \frac{1}{\Phi(z/\sigma_z) \Delta x \sqrt{2\pi\sigma_z^2}} \exp \left[-\frac{(z - z')^2}{2\sigma_z^2} \right], \quad (36)$$

for $\sigma_z = d/2$ the coarse-graining width, Δx the downslope extent over which images were captured, and Φ the cumulative distribution function of the standard normal distribution, accounting for the impossibility of detecting particles below the base's surface.

S9. Statistical Tools

S9.1. Standard Errors

In sections S6.2, S6.3, S7.2, and S7.3, the standard error in the sample mean (or mean standard error) over repeated measurements $(y_j)_{j=1}^n$, with mean \bar{y} , is defined by

$$\sigma_m = \frac{1}{\sqrt{n}} \left[\sqrt{\frac{1}{n-1} \sum_{j=1}^n (y_j - \bar{y})^2} \right]. \quad (37)$$

Considering measurements as independent and identically distributed random variables, $n\sigma_m^2$ is an unbiased estimator for the variance of the distribution from which they are taken, provided the latter is finite, and so σ_m^2 is an unbiased estimator for the variance of \bar{y} , considered as a random variable. Under this model, assuming certain regularity conditions, the central limit theorem implies that \bar{y} is taken from an approximately normal distribution, with true expectation μ equal to the expectation of y_j . Consequently, σ_m is a typical error for the estimation of μ by \bar{y} , in the sense that it's the scale by which confidence intervals for μ can be derived from the percentage points of the standard normal distribution. For example, $\bar{y} \pm \sigma_m$ is an approximate 68 % confidence interval for μ , while $\bar{y} \pm 2\sigma_m$ is an approximate 95 % confidence interval.

S9.2. Fitting a Model's Free Parameters

In seeking the free parameter values for which a model's predictions \hat{P}_F^0 best fit our observations P_F^0 , we are concerned with the ratio between predictions and observations, and wish to penalise underestimates by a given factor as much as overestimates by that factor. Rather than considering the arithmetic error $P_F^0 - \hat{P}_F^0$, which places excessive weight on predictions' agreement with large values P_F^0 , or the fractional error $1 - \hat{P}_F^0/P_F^0$, which penalises overestimates more than underestimates, we therefore consider the logarithmic error $\ln(P_F^0/\hat{P}_F^0)$. To penalise large errors more than small errors, we take a quadratic loss function, and seek to minimise

$$\epsilon = \exp \left[\sqrt{\frac{1}{N} \sum \ln^2 \left(P_F^0 / \hat{P}_F^0 \right)} \right], \quad (38)$$

the geometric standard error over the $N = 57$ predictions. This may be interpreted as a typical factor by which predictions are greater or lesser than observations.

To understand this parameter fitting within a statistical framework, and to make rigorous the sense in which ϵ is 'typical', we note that our measurements are subject to a large number of approximately independent multiplicative errors, so that observations P_F^0 may be expected to be approximately log-normally distributed about the predictions $\hat{P}_F^0(\theta_0)$ of an accurate model with accurate free parameter value θ_0 . Under this statistical model, the likelihood may be written as a function of the free parameter θ and the log-normal distribution's shape parameter σ as

$$\mathcal{L}(\theta, \sigma | \ln P_F^0) = \prod \frac{1}{\sqrt{2\pi\sigma^2}} \exp \left[-\frac{\ln^2(P_F^0/\hat{P}_F^0(\theta))}{2\sigma^2} \right]. \quad (39)$$

By considering $\ln \mathcal{L}$, we can see that choosing the parameter value that minimises $\ln \epsilon$, and so ϵ , is equivalent to using the maximum likelihood estimator for θ . Similarly, the maximum likelihood estimator for σ^2 is $\ln^2 \epsilon$, equal to the mean square value of $\ln(P_F^0/\hat{P}_F^0)$. Under this model, with these parameters, ϵ will be the typical geometric error in the same sense that σ_m is typical in section S9.1: considering the percentage points of the normal distribution, 68 % of observations P_F^0 will be within $\epsilon^{\pm 1} \hat{P}_F^0$, while 95 % will be within $\epsilon^{\pm 2} \hat{P}_F^0$.

S9.3. The Akaike Information Criterion

To compare physical models with differing numbers of free parameters, we use the Akaike information criterion. For each model predicting \hat{P}_F^0 , we consider the statistical model discussed in section S9.2, in which $\ln P_F^0$ is normally distributed about $\ln \hat{P}_F^0$ with constant variance σ^2 . We note that if the physical model has a number k of free parameters, the associated statistical model has $k + 1$ free parameters, due to the additional free parameter σ^2 . Considering the likelihood \mathcal{L} for this model, as defined in equation (39),

the value of the Akaike information criterion is therefore (Akaike, 1971)

$$AIC = 2(k + 1 - \ln(\max \mathcal{L})). \quad (40)$$

The Akaike information criterion balances each of the five models' goodness of fit against the number of parameters varied to achieve that fit, with $AIC/2$ a good estimator for the information lost in describing the true data-generating process by the model under consideration. Akaike (1974) makes this rigorous, for the Kullback-Liebler sense of information (Kullback & Liebler, 1951), but in brief the model minimising AIC is preferred in an information theoretic sense, with $RL = \exp[(\min AIC - AIC)/2]$ the relative likelihood of any other model (Akaike, 1978).

Of the existing models for a flow's seismic signal, as described in section 1.2 and implemented in section 3.3, the 'thin-flow' model of Farin et al. (2019) is strongly preferred by the Akaike information criteria. All models' AIC and RL values are listed in Table S1. Results are identical when using Hurvich and Tsai (1989)'s correction to the Akaike information criterion, which avoids bias for finite sample sizes, under certain regularity conditions.

S10. The Green's Function's Effect on Signals' Energy and Relative Amplitude

Here, we use our experimental seismic signals to show that a signal's Green's function affects certain seismic properties that previous authors have used to describe geophysical flows directly: the rate of seismic energy emission and the relative amplitudes of different landquake signals with the same source and receiver locations.

For our experiments, the Green's function appears via equation (12) of the main text, which relates the basal forces exerted by the flow to the accelerations they caused and indicates that, on a larger, denser, stiffer, or more lossy plate, the same force would result in smaller accelerations and hence a smaller seismic signal. Similarly, working from the derivation of this equation in S7, the total high-frequency seismic power transferred by the flow to the plate is given in terms of the basal force's power spectral density P_F by

$$\Pi_s \approx \frac{1}{4\sqrt{\rho_p H D}} \int_{1 \text{ kHz}}^{\infty} P_F(f) df, \quad (41)$$

dependent on plate density ρ_p , thickness H , and bending moment D . The proportion of flow energy dissipated by seismic emission is therefore a function of basal properties rather than of flow properties alone.

Furthermore, the Green's functions for seismic signals will depend differently on frequency f , so that basal properties

Table S1. *Model comparison with the Akaike information criterion.* For each of the existing physical models described in section 1.2, we list the number k of free parameters in its implementation in section 3.3; the value AIC of the Akaike information criterion for its associated statistical model; and this model's relative likelihood RL .

Model	k	AIC	RL
Kean et al. (2015)	1	204	6×10^{-17}
Lai, Tsai, Lamb, Ulizio, and Beer (2018)	0	284	3×10^{-34}
Farin et al. (2019) 'thick-flow'	1	181	7×10^{-12}
Farin et al. (2019) 'thin-flow'	1	129	1
Bachelet et al.	1	199	8×10^{-16}

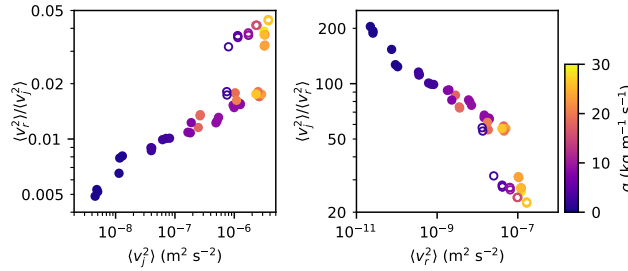


Figure S6. Comparison between the mean squared seismic velocities $\langle v_j^2 \rangle$ observed in our experiments and the mean squared velocities $\langle v_r^2 \rangle$ that would be observed in an idealised geophysical context. For the latter, we took $\rho_g = 2500 \text{ kg m}^{-3}$, $c_s = 1 \text{ km s}^{-1}$, and $r = 1 \text{ m}$ in equation (42), but other values would change only the prefactor. Colours indicate each experiment's mass flux q per unit channel width, and unfilled symbols represent experiments for which the flow was in the transitional regime.

will affect even the relative signal amplitudes of different flows with the same Green's function. For illustration, we consider the vertical velocity response of a surficial receiver to a vertical, surficial point force, on an isotropic, homogeneous, perfectly elastic half-space with Poisson ratio 0.25, material density ρ_g and shear wave velocity c_s . For large source-receiver separation r , at leading order, Miller and Pursey (1954) showed the power spectral density P_{v_r} of this response to be related to the power spectral density P_F of the vertical basal force by

$$P_{v_r}(f) = \frac{1.20f^3}{\rho_g^2 c_s^5 r} P_F(f), \quad (42)$$

which we compare to the mean velocity power spectral density over the accelerometers in our experiments,

$$\bar{P}_{v_j}(f) = \frac{1}{4\Delta t} \sum_{j=1}^4 \left(\frac{|\tilde{a}_j(f)|}{2\pi f} \right)^2 \approx \frac{\mathcal{P}Q}{16\pi(\rho_p H)^{3/2} XY \sqrt{D} f} P_F(f). \quad (43)$$

The mean squared velocity at the receiver, being the integral of $P_{v_r}(f)$ over all f , will clearly be more sensitive to the corner frequency f_c of P_F than were the mean squared velocities observed in our experiments. Figure S6 shows the consequence: approximating mean squared velocities by integrating (42) and (43) between 1 kHz and f_c , there is no constant conversion factor between the mean square velocities observed in our experiments and those that would be observed if the same flows applied the same forces in an idealised geophysical context. Even among signals with the same source and receiver locations, the Green's function determines the ratios between different signals' amplitudes, so that a signal must be properly deconvolved to infer the properties of a flow's forces.

Movie S1.

Example of footage captured by the high-speed camera at the channel wall, as described in section 2.1. Footage was captured during the period of steady flow of an experiment at a channel incline $\tan \theta = 0.44$, with a release gate height $h_g = 5 \text{ mm}$. The movie is a 0.5 s excerpt, vertically cropped and slowed by a factor of 20.

Movie S2.

Illustration of particle tracking velocimetry. Footage was captured during the period of steady flow of an experiment at a channel incline $\tan \theta = 0.48$, with a release gate height $h_g = 20 \text{ mm}$. Superposed red dots indicate the particle centres located by the algorithm described in S8, while blue

lines indicate particle trajectories reconstructed after that algorithm's particle tracking and velocity smoothing.

References

- Akaike, H. (1971). *Determination of the number of factors by an extended maximum likelihood principle* (Tech. Rep.). Inst. Statist. Math.
- Akaike, H. (1974). A new look at the statistical model identification. *IEEE Transactions on Automatic Control*, 19(6), 716–723. Retrieved from <https://link.springer.com/content/pdf/10.1007%2F978-1-4612-1694-0.pdf>
- Akaike, H. (1978). On the likelihood of a time series model. *Journal of the Royal Statistical Society. Series D (The Statistician)*, 27(3/4), 217–235. Retrieved from <http://www.jstor.org/stable/2988185>
- Arran, M. I., Mangeney, A., de Rosny, J., Farin, M., Toussaint, R., & Roche, O. (2021). *Laboratory landquakes, v1.0*. Zenodo. doi: 10.5281/zenodo.4044233
- Babic, M. (1997). Average balance equations for granular materials. *International Journal of Engineering Science*, 35(5), 523–548. Retrieved from <http://www.sciencedirect.com/science/article/pii/S0020722596000948> doi: 10.1016/S0020-7225(96)00094-8
- Bertrand, J. (1878). Sur l'homogénéité dans les formules de physique. *Comptes rendus hebdomadaires des séances de l'Académie des sciences*, 86(15), 916–920.
- Buckingham, E. (1914). On physically similar systems; illustrations of the use of dimensional equations. *Physical Review*, 4(4), 345–376.
- Ciarlet, P. G. (1997). Chapter 1 - linearly elastic plates. In P. G. Ciarlet (Ed.), *Mathematical elasticity* (Vol. 27, p. 3–127). Elsevier. Retrieved from <http://www.sciencedirect.com/science/article/pii/S0168202497800070> doi: 10.1016/S0168-2024(97)80007-0
- Farin, M., Tsai, V. C., Lamb, M. P., & Allstadt, K. E. (2019). A physical model of the high-frequency seismic signal generated by debris flows. *Earth Surface Processes and Landforms*, 44(13), 2529–2543. Retrieved from <https://onlinelibrary.wiley.com/doi/abs/10.1002/esp.4677> doi: 10.1002/esp.4677
- Hertz, H. R. (1881). Über die berührung fester elastischer körper. *Journal für die reine und angewandte Mathematik*, 92, 156–171. Retrieved from <https://home.uni-leipzig.de/pwm/web/download/Hertz1881.pdf>
- Hurvich, C. M., & Tsai, C.-L. (1989). Regression and time series model selection in small samples. *Biometrika*, 76(2), 297–307. Retrieved from <https://doi.org/10.1093/biomet/76.2.297> doi: 10.1093/biomet/76.2.297

- Kean, J. W., Coe, J. A., Coviello, V., Smith, J. B., McCoy, S. W., & Arattano, M. (2015). Estimating rates of debris flow entrainment from ground vibrations. *Geophysical Research Letters*, 42(15), 6365–6372. Retrieved from <https://agupubs.onlinelibrary.wiley.com/doi/abs/10.1002/2015GL064811> doi: 10.1002/2015GL064811
- Kullback, S., & Leibler, R. A. (1951). On information and sufficiency. *Ann. Math. Statist.*, 22(1), 79–86. Retrieved from <https://doi.org/10.1214/aoms/1177729694> doi: 10.1214/aoms/1177729694
- Lai, V. H., Tsai, V. C., Lamb, M. P., Ulizio, T. P., & Beer, A. R. (2018, 06). The seismic signature of debris flows: Flow mechanics and early warning at Montecito, California. *Geophysical Research Letters*, 45(11), p5528–5535. doi: 10.1029/2018GL077683
- Love, A. E. H., & Darwin, G. H. (1888). XVI. the small free vibrations and deformation of a thin elastic shell. *Philosophical Transactions of the Royal Society of London. (A.)*, 179, 491–546. Retrieved from <https://royalsocietypublishing.org/doi/abs/10.1098/rsta.1888.0016> doi: 10.1098/rsta.1888.0016
- McLaskey, G. C., & Glaser, S. D. (2010). Hertzian impact: Experimental study of the force pulse and resulting stress waves. *The Journal of the Acoustical Society of America*, 128(3), 1087–1096. Retrieved from <https://asa.scitation.org/doi/abs/10.1121/1.3466847> doi: 10.1121/1.3466847
- Michlmayr, G., & Or, D. (2014, October 01). Mechanisms for acoustic emissions generation during granular shearing. *Granular Matter*, 16(5), 627–640. Retrieved from <https://doi.org/10.1007/s10035-014-0516-2> doi: 10.1007/s10035-014-0516-2
- Miller, G. F., & Pursey, H. (1954). The Field and Radiation Impedance of Mechanical Radiators on the Free Surface of a Semi-Infinite Isotropic Solid. *Proceedings of the Royal Society of London A: Mathematical, Physical and Engineering Sciences*, 223(1155), 521–541. Retrieved from <http://rspa.royalsocietypublishing.org/content/223/1155/521> doi: 10.1098/rspa.1954.0134